

## Continuous-time Monte Carlo and spatial ordering in driven lattice gases: Application to driven vortices in periodic superconducting networks

Violeta Gotcheva,\* Yanting Wang,<sup>†</sup> Albert T. J. Wang,<sup>‡</sup> and S. Teitel

*Department of Physics and Astronomy, University of Rochester, Rochester, New York 14627, USA*

(Received 21 March 2005; published 4 August 2005)

We consider the two-dimensional (2D) classical lattice Coulomb gas as a model for magnetic field induced vortices in 2D superconducting networks. Two different dynamical rules are introduced to investigate driven diffusive steady states far from equilibrium as a function of temperature and driving force. The resulting steady states differ dramatically depending on which dynamical rule is used. We show that the commonly used driven diffusive Metropolis Monte Carlo dynamics contains unphysical intrinsic randomness that destroys the spatial ordering present in equilibrium (the vortex lattice) over most of the driven phase diagram. A continuous time Monte Carlo (CTMC) method is then developed, which results in spatially ordered driven states at low temperature in finite sized systems. We show that CTMC is the natural discretization of continuum Langevin dynamics, and argue that it gives the correct physical behavior when the discrete grid represents the minima of a periodic potential. We use detailed finite size scaling methods to analyze the spatial structure of the steady states. We find that finite size effects can be subtle and that very long simulation times can be needed to arrive at the correct steady state. For particles moving on a triangular grid, we find that the ordered moving state is a transversely pinned smectic that becomes unstable to an anisotropic liquid on sufficiently large length scales. For particles moving on a square grid, the moving state is a similar smectic at large drives, but we find evidence for a possible moving solid at lower drives. We find that the driven liquid on the square grid has long range hexatic order, and we explain this as a specifically nonequilibrium effect. We show that, in the liquid, fluctuations about the average center of mass motion are diffusive in both the transverse and longitudinal directions.

DOI: [10.1103/PhysRevB.72.064505](https://doi.org/10.1103/PhysRevB.72.064505)

PACS number(s): 74.25.Qt, 74.81.Fa, 05.10.Ln

### I. INTRODUCTION

While the theory of phase transitions of systems in thermodynamic equilibrium is a well established and mature area of statistical physics, much less is established about analogous critical behavior in driven steady states far from equilibrium. As has been the case in the study of equilibrium phase transitions, the use of lattice models, in which the degrees of freedom are constrained to sit on the sites of a discrete periodic grid, has led to analytical simplifications and greater accuracy in numerical simulations for investigating such steady states, as compared to corresponding continuum models.<sup>1</sup> One advantage of a lattice gas model for numerical simulations of driven interacting many-body systems is that particles hop in discrete jumps. If a particle sits in a local potential minimum, the lattice gas dynamics can allow the particle to hop over the energy barrier out of the minimum in a single move. In contrast, in continuum simulations such as molecular dynamics, considerable simulation time can be wasted at low temperatures waiting for a thermal excitation that will excite the particle over the energy barrier. The lattice gas method can therefore hope to simulate out to much longer effective times, and focus on effects due to many-body interactions rather than single body potentials.

One of the first, and still one of the most commonly used, numerical methods to simulate driven steady states of a lattice gas is the driven diffusive Monte Carlo method. This method, introduced by Katz, Lebowitz, and Spohn,<sup>2</sup> extends familiar equilibrium Monte Carlo methods to the case of driven nonequilibrium states. The key idea of this method is

to include the work done by the driving force on a moved particle, in addition to the change in interaction energy, when computing the energy difference to use in the Monte Carlo test for making moves. Such a term biases motion in the direction of the driving force, and, with the use of periodic boundary conditions, results in a steady state with a finite particle current. This algorithm, which satisfies local detailed balance for individual particle moves, seeks to model diffusively moving particles in the limit where motion is dominated by thermal activation over energy barriers, rather than microscopic dynamics. The hope is that the main qualitative features of the driven steady states, and possible phase transitions between them, will be independent of the details of the microscopic dynamics, and so will be captured by this algorithm.

However, unlike equilibrium simulations, where *any* dynamics that satisfies detailed balance is sufficient to generate the correct equilibrium Gibbs ensemble and so equilibrium averages are in principal independent of the microscopic dynamics, there is no such guarantee for nonequilibrium states. Even for sets of dynamics that would appear to lie within the same dynamic “universality class”<sup>3</sup> from the viewpoint of symmetry and conserved quantities, averages in driven steady states far from equilibrium may conceivably be qualitatively, not just quantitatively, different.

In this work we test this notion explicitly by considering two different versions of driven diffusive Monte Carlo dynamics, both intended to model the overdamped diffusive limit. We consider first (i) driven diffusive Metropolis Monte Carlo (DDMMC) dynamics<sup>1,2</sup>, where the standard Metropo-

lis method is used to select attempted excitations and decide whether or not to accept them. We then consider (ii) driven diffusive continuous time Monte Carlo (CTMC) dynamics, where the continuous time Monte Carlo method<sup>4,5</sup> is used to make a rejectionless dynamics. We believe that our work is the first application of continuous time Monte Carlo in the context of driven diffusive problems. We apply these methods to the problem of the driven two-dimensional (2D) classical one component lattice Coulomb gas, which serves as a model for logarithmically interacting, magnetic field induced, vortices in periodic 2D superconducting networks.<sup>6</sup> We consider both the cases of a triangular and a square grid of sites. This model is of interest because it allows one to consider the effect of a uniform driving force on a system which has spatially ordered states in equilibrium (the vortex lattice), in contrast to simpler nearest-neighbor Ising-like lattice gas models,<sup>7</sup> which, in general, have no such periodic spatial order.

We find that our two dynamics result in dramatically different driven steady states, when the system is acted upon by a uniform applied force  $F$ . We find that over most of the  $T$ - $F$  phase diagram, the DDMMC method results in a spatially disordered moving steady state with a very short translational correlation length. We argue that this behavior is due to intrinsic randomness in the DDMMC algorithm, that is sufficient to disorder the moving system even at  $T=0$ . In contrast, we find that the CTMC method, at least for finite size systems, can result in spatially ordered moving steady states, as well as orientationally ordered moving liquids. We demonstrate that the CTMC method is the correct discretization of diffusive Langevin dynamics in a certain limit, and argue that it more generally describes motion when the discrete grid is thought of as representing the minima of a one body periodic potential, and the energy barriers of this potential are large compared to the energy change of hopping between minima. Thus we believe that CTMC is not only a more interesting dynamics, but also a more physically correct one. For CTMC dynamics, we carry out detailed finite size scaling analyses of our ordered steady states, and show that there can be subtle finite size effects due to diverging correlation lengths at low temperatures. We also show that exceedingly long simulations are needed, in some cases, in order to arrive at the correct steady state distribution.

The remainder of this paper is organized as follows. In Sec. II we define in detail our Coulomb gas model and our two lattice gas dynamics. We discuss qualitative behaviors to be expected at low temperatures, and define the observables we will measure. In Sec. III we present the results of our simulations on a triangular grid of sites. We show the phase diagrams of both the DDMMC and CTMC for a system of a given finite size, and demonstrate the dramatic difference between them. We then focus the remainder of our work on CTMC. We carry out detailed finite size scaling analyses to study the structural order of the moving steady states in both the high drive and low drive limits. At low temperature we find an ordered moving smectic state, however, we argue that this state is ultimately unstable to a liquid on sufficiently large length scales. We also present results for dynamic behavior, studying the average velocity of the system and the diffusion of the system about its center of mass motion. In

Sec. IV we present our results for simulations on a square grid of sites. We study several specific points in the phase diagram representative of the high drive and low drive limits. Unlike for the triangular grid, we find that the structure of the ordered moving state appears to have different periodicities at different driving forces. We carry out finite size scaling to investigate the stability of the ordered states in the large size limit. We show that, unlike the liquid state in equilibrium, the liquid driven steady state possesses long range hexatic orientational order. In Sec. V we discuss our results and present our conclusions.

Some aspects of this work, focusing on the differences between DDMMC and CTMC and the structural order of driven states on the triangular grid, have previously appeared as a letter.<sup>8</sup> The detailed discussion of the phase diagram on the triangular grid, the finite size scaling analyses, the discussion of dynamical behavior, and all results for the square grid, are new to the current work.

## II. MODEL AND METHODS

### A. Coulomb gas model

Our model is a classical one component lattice Coulomb gas of 2D interacting charges, which may be taken as a model for interacting vortices in a 2D superconducting network.<sup>6</sup> The charges are constrained to sit on the discrete sites  $i$  of a periodic 2D grid. If the basis vectors of the grid are  $\{\hat{a}_1, \hat{a}_2\}$ , we take the grid to have finite length  $L_\mu$  in direction  $\hat{a}_\mu$  and we take periodic boundary conditions in both directions. The Hamiltonian is given by<sup>6</sup>

$$\mathcal{H} = \frac{1}{2} \sum_{i,j} (n_i - f)G(\mathbf{r}_i - \mathbf{r}_j)(n_j - f), \quad (1)$$

where the sum is over all pairs of sites  $i, j$  of the grid,  $n_i \in \{0, 1\}$  is the integer charge on site  $i$ ,  $-f$  is a fixed uniform neutralizing background charge, and  $G(\mathbf{r})$  is the 2D lattice Coulomb potential which solves

$$\Delta^2 G(\mathbf{r}) = -2\pi\delta_{\mathbf{r},0}, \quad (2)$$

where  $\Delta^2$  is the discrete Laplacian for the grid. Defining  $\Delta^2$  appropriate to periodic boundary conditions results in a  $G(\mathbf{r})$  that satisfies periodic boundary conditions. For separations large compared to the grid spacing, but small compared to the grid length ( $1 \ll |\mathbf{r}| \ll L$ ), one has  $G(\mathbf{r}) \simeq -\ln|\mathbf{r}|$ . The condition that the total energy remain finite imposes the charge neutrality condition

$$\sum_i n_i = fL_1L_2 \equiv N_c. \quad (3)$$

We will consider first the case of a triangular grid of sites. Here the basis vectors are

$$\begin{aligned} \hat{a}_1 &= \hat{x}, \\ \hat{a}_2 &= \frac{1}{2}\hat{x} + \frac{\sqrt{3}}{2}\hat{y} \end{aligned} \quad (4)$$

and the sites  $i$  of the grid are specified by the position vectors

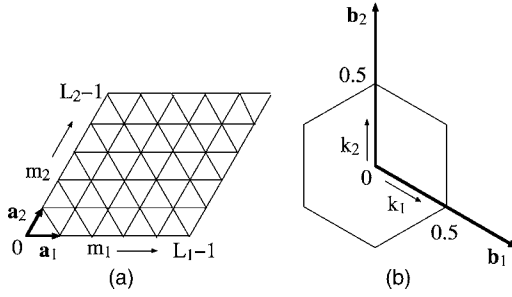


FIG. 1. (a) Triangular grid of size  $L_1 \times L_2$  with basis vectors  $\hat{a}_1$  and  $\hat{a}_2$ . (b) Reciprocal space to the triangular grid, with basis vectors  $\mathbf{b}_1$  and  $\mathbf{b}_2$ . Allowed wave vectors for Fourier transforms of real space quantities can be restricted to the hexagonal first Brillouin zone shown in (b).

$$\mathbf{r}_i = m_1 \hat{a}_1 + m_2 \hat{a}_2, \quad (5)$$

$$m_\mu \in \{0, 1, \dots, L_\mu - 1\}.$$

The geometry of this real space grid is illustrated in Fig. 1(a).

The solution to Eq. (2) will be given in terms of its Fourier transform. The basis vectors of the reciprocal to the grid in Fourier transform space are then

$$\begin{aligned} \mathbf{b}_1 &= 2\pi\hat{x} - \frac{2\pi}{\sqrt{3}}\hat{y}, \\ \mathbf{b}_2 &= \frac{4\pi}{\sqrt{3}}\hat{y}, \end{aligned} \quad (6)$$

and the allowed wave vectors consistent with periodic boundary conditions are given by

$$\begin{aligned} \mathbf{k} &= k_1 \mathbf{b}_1 + k_2 \mathbf{b}_2, \\ k_\mu &\in \left\{ 0, \frac{1}{L_\mu}, \dots, \frac{L_\mu - 1}{L_\mu} \right\}. \end{aligned} \quad (7)$$

Equivalently, one could translate the above wavevectors by an appropriate linear combination of the basis vectors  $\{\mathbf{b}_1, \mathbf{b}_2\}$  so that they all lie in the hexagonal shaped first Brillouin zone of the reciprocal grid. The geometry of these allowed wavevectors is illustrated in Fig. 1(b).

Defining  $\hat{a}_3 \equiv \hat{a}_1 - \hat{a}_2$ , the discrete Laplacian for the triangular grid is given by

$$\Delta^2 G(\mathbf{r}) \equiv c \sum_{\mu=1}^3 [G(\mathbf{r} + \hat{a}_\mu) - 2G(\mathbf{r}) + G(\mathbf{r} - \hat{a}_\mu)] \quad (8)$$

with  $c$  an appropriate geometrical constant to give the correct continuum limit. Taking the Fourier transform of the above, we find that the solution to Eq. (2) is given by<sup>6,9</sup>

$$G(\mathbf{r}) = \frac{\pi}{cN} \sum_{\mathbf{k} \neq 0} \frac{e^{i\mathbf{k} \cdot \mathbf{r}}}{3 - \cos(\mathbf{k} \cdot \hat{a}_1) - \cos(\mathbf{k} \cdot \hat{a}_2) - \cos(\mathbf{k} \cdot \hat{a}_3)}, \quad (9)$$

where  $N = L_1 L_2$  is the number of sites in the grid, and the sum is over all the allowed wave vectors of Eq. (7). The correct

value of the geometric constant is  $c = 1/\sqrt{3}$ . However, in order to compare with previous work done on this model,<sup>6</sup> we will make the choice  $c = 2/3$ . This difference amounts only to a rescaling of the temperature.

We will also discuss the case of a square grid of sites. Here the real space basis vectors of the grid are  $\{\hat{a}_1, \hat{a}_2\} = \{\hat{x}, \hat{y}\}$ , the basis vectors of the reciprocal space are  $\{\mathbf{b}_1, \mathbf{b}_2\} = \{2\pi\hat{x}, 2\pi\hat{y}\}$ , and the lattice Coulomb potential is given by<sup>6,9</sup>

$$G(\mathbf{r}) = \frac{2\pi}{N} \sum_{\mathbf{k} \neq 0} \frac{e^{i\mathbf{k} \cdot \mathbf{r}}}{2 - \cos(\mathbf{k} \cdot \hat{a}_1) - \cos(\mathbf{k} \cdot \hat{a}_2)}. \quad (10)$$

## B. Lattice gas dynamics

Our goal is to simulate the nonequilibrium steady states of the lattice Coulomb gas when driven by a uniform applied force  $\mathbf{F}$ . For equilibrium simulations, any dynamical rule that satisfies detailed balance will converge to the correct equilibrium ensemble; the details of the dynamics may effect the speed of convergence, but they are otherwise irrelevant for computing time-independent thermodynamic averages. For nonequilibrium steady states, however, even time-independent averages may depend on the details of the microscopic dynamics. Here we consider two different microscopic dynamics for the simple case of over damped diffusively moving particles (the simplest case in the classification scheme of dynamic critical phenomena by Halperin and Hohenberg<sup>3</sup>). Both dynamics involve single-particle moves only. We find that, for finite size systems, the resulting steady states for these two dynamics can be qualitatively different.

### 1. Driven diffusive metropolis Monte Carlo (DDMMC)

The first lattice gas dynamics we consider is the commonly used driven diffusive Metropolis Monte Carlo<sup>1,2</sup> (DDMMC) dynamics. This algorithm was introduced as a simple modification of ordinary equilibrium Metropolis Monte Carlo. It was intended to model the steady states of a driven system in the limit where motion is dominated by thermal activation over energy barriers, and so presumably is not very sensitive to microscopic details. The DDMMC algorithm is defined as follows. At each step of the simulation a charge  $n_i = 1$  is selected at random, and the charge is then moved a test displacement  $\Delta\mathbf{r}$  to a randomly chosen nearest-neighbor site. For the triangular grid,  $\Delta\mathbf{r}$  is chosen with equal probability from the six possible directions  $\pm\hat{a}_\mu$ ,  $\mu = 1, 2, 3$ . If  $\mathcal{H}_{\text{old}}$  and  $\mathcal{H}_{\text{new}}$  are the interaction energies, Eq. (1), of the system before and after this test move is made, one computes the energy difference

$$\Delta U = \mathcal{H}_{\text{new}} - \mathcal{H}_{\text{old}} - \mathbf{F} \cdot \Delta\mathbf{r}, \quad (11)$$

where the last term is the work done by the applied force on the moved charge. This test move is then accepted or rejected according to the usual Metropolis criterion

$$\begin{aligned} &\text{accept if } e^{-\Delta U/T} > r, \\ &\text{reject if otherwise,} \end{aligned} \quad (12)$$

where  $r$  is a random variable uniformly distributed on  $[0, 1)$ . One pass of  $N_c$  such steps equals one unit of simulation time. The term in Eq. (11) proportional to the force  $\mathbf{F}$  biases moves parallel to  $\mathbf{F}$  and, in conjunction with the periodic boundary conditions, will in general set up a steady state with a finite current of particles moving parallel to  $\mathbf{F}$ . Time-independent averages are computed in the usual Monte Carlo way, as a direct average over configurations sampled every  $N_{\text{pass}}$  passes.

## 2. Driven diffusive continuous time Monte Carlo (CTMC)

The second dynamics we consider, and the one which is used for the main part of our work presented here, we call driven diffusive continuous time Monte Carlo dynamics (CTMC). The algorithm is defined as follows. Starting from a particular initial configuration, we denote by  $(i\alpha)$  the single particle move of a charge  $n_i=1$  on site  $\mathbf{r}_i$ , to its nearest-neighbor site in direction  $\hat{\alpha}$ . For the triangular grid,  $\hat{\alpha} \in \{\pm\hat{a}_1, \pm\hat{a}_2, \pm\hat{a}_3\}$ . For a grid in which each site has  $z$  nearest neighbors, the total number of such possible single particle moves is  $zN_c$ . For each such move, we compute the energy change  $\Delta U_{i\alpha}$  according to Eq. (11), and define a probability rate for making this move

$$W_{i\alpha} = W_0 e^{-\Delta U_{i\alpha}/2T}, \quad (13)$$

where  $1/W_0$  sets the unit of time. Note that the above rates, as well as the Metropolis rates of DDMMC set by Eq. (12), obey a local detailed balance. If  $s$  is an initial state, and  $s'$  is the state reached from  $s$  by making the single particle move  $(i\alpha)$ , then,

$$\frac{W(s \rightarrow s')}{W(s' \rightarrow s)} = e^{-\Delta U_{i\alpha}/T}. \quad (14)$$

Although systems out of equilibrium do not in general need to satisfy detailed balance, local detailed balance is physically reasonable if we wish to regard each charge as moving in a local potential determined by its interactions with the other charges and with the applied force.

Having specified the rates of Eq. (13), we determine which move to make by regarding all  $zN_c$  of the possible single particle moves as independent Poisson processes. The probability that the next move will be  $(i\alpha)$  is then

$$P_{i\alpha} = \frac{W_{i\alpha}}{\sum_{(j\beta)} W_{j\beta}} \quad (15)$$

and the average time it takes to make this move is

$$\Delta t = \frac{1}{W_{\text{tot}}} \equiv \frac{1}{\sum_{(j\beta)} W_{j\beta}}. \quad (16)$$

We thus make a move by sampling the probability distribution  $P_{i\alpha}$  of Eq. (15), and then update the simulation clock by the amount  $\Delta t$  of Eq. (16). Averages of observables  $O$  are computed as

$$\langle O \rangle = \frac{1}{\tau} \int O(t) dt = \frac{1}{\tau} \sum_s O_s \Delta t_s, \quad (17)$$

where  $s$  labels the steps of the simulation,  $O_s$  is the value of  $O$  in the configuration at step  $s$ ,  $\Delta t_s \equiv t_{s+1} - t_s$  is the time spent in the configuration at step  $s$  according to the simulation clock, and  $\tau = \sum_s \Delta t_s$  is the total time of the simulation. As in DDMMC, we will refer to  $N_c$  simulation steps as one *pass* through the system.

The above algorithm is a straightforward extension of the equilibrium continuous time Monte Carlo algorithm,<sup>5</sup> but we believe that this is its first application in the context of driven nonequilibrium steady states. The method was first introduced as the “ $n$ -fold way” for spin models.<sup>4</sup> It owes its name to the continuous variations in the time steps  $\Delta t_s$ , which vary from configuration to configuration, according to the energy barriers present in each configuration. It is a rejectionless algorithm designed to speed up equilibration at low temperatures. Rather than waste many rejected moves until a rare acceptance takes one up and over an energy barrier, the energy barriers  $\Delta U_{i\alpha}$  themselves set the time scale for each move, which then happens in a single simulation step. Simulation clock times can vary over orders of magnitude as either  $T$  or the height of the energy barriers vary.

In CTMC there are many possible choices for the rates  $W_{i\alpha}$  that would satisfy local detailed balance. In Appendix A we show that the particular choice of Eq. (13), with  $W_0 = cDT$  ( $D$  is the diffusion constant), is the natural discretization to a periodic grid of sites of over damped continuum Langevin dynamics, and that the continuum limit is reached when  $\Delta U_{i\alpha} \ll T$ . Our simulations, however, being generally at low  $T$  or large  $\mathbf{F}$ , are mostly in the opposite limit of  $\Delta U_{i\alpha} \gtrsim T$ . To see what physical situation this limit corresponds to, consider a single particle moving on a one dimensional grid of sites, in a driving force  $F$ . According to the CTMC algorithm, the average distance traveled in one step is

$$\langle \Delta x \rangle = \frac{e^{F/2T} - e^{-F/2T}}{e^{F/2T} + e^{-F/2T}}, \quad (18)$$

while the average time for this step is given by

$$\frac{1}{\Delta t} = W_{\text{tot}} = W_0 [e^{F/2T} + e^{-F/2T}], \quad (19)$$

leading to an average velocity

$$\langle v \rangle = \frac{\langle \Delta x \rangle}{\Delta t} = 2W_0 \sinh(F/2T). \quad (20)$$

At low ratios of  $F/T$  the velocity is linear in the applied force  $\langle v \rangle \approx W_0 F/T$ ; at large  $F/T$ , the velocity grows exponentially,  $\langle v \rangle \approx W_0 e^{F/2T}$ . We can compare the above result to that of an over damped particle moving in a continuum “washboard potential”  $U(x) = -U_0 \cos(2\pi x) - Fx$ , which has been studied by Ambegaokar and Halperin in the context of a driven Josephson junction.<sup>10</sup> The average velocity that they find agrees exactly with Eq. (20) above, if one is in the limit  $T \ll 2U_0$  and  $F < 2\pi U_0$ , and one identifies



$$W_0 = 2\pi U_0 D \sqrt{1 - \gamma^2} e^{-2U_0[\sqrt{1 - \gamma^2} + \gamma \sin^{-1} \gamma]/T}, \quad (21)$$

where  $D$  is the diffusion constant and  $\gamma \equiv F/2\pi U_0$ . For small  $\gamma$  the above  $W_0$  reduces to a form independent of the drive  $F$ ,

$$W_0 \approx 2\pi U_0 D e^{-2U_0/T}, \quad \text{when } F \ll 2\pi U_0, \quad (22)$$

which is the rate for activation over an energy barrier of  $2U_0$ . CTMC thus describes the limit where the grid sites represent the minima of a periodic pinning potential, and the applied force is weak enough that motion is due to thermal activation of particles, one at a time, over the barriers of this periodic potential. It is unclear<sup>11</sup> if CTMC can qualitatively describe the very large drive limit  $F \gg U_0$ , where the washboard potential loses its local minima parallel to  $\mathbf{F}$ , and the average velocity again becomes proportional to  $\mathbf{F}$ . For the results reported in the following sections we will measure time in units where  $W_0 = 1$ , independent of the temperature  $T$  or driving force  $F$ .

### 3. Behavior at low temperature

To get a better feel for the behavior of the above two lattice gas dynamic algorithms, we can consider their behavior at low temperature. In the limit  $T \rightarrow 0$ , the DDMMC will reject all moves except those that lower the energy, i.e.,  $\Delta U_{i\alpha} < 0$ . If one starts initially in the  $F=0$  ground state and increases  $F$ , all moves will be rejected until  $F$  reaches a critical value  $F_c$  equal to the interaction energy associated with moving one charge forward one grid spacing parallel to  $\mathbf{F}$ . The ordered ground-state charge lattice will therefore be pinned with  $\langle \mathbf{v} \rangle = 0$  for  $F < F_c$ , and moving with  $\langle \mathbf{v} \rangle$  finite for  $F > F_c$ .

Next we consider DDMMC at  $T=0$  with  $F \gg F_c$ , so that the work done by the force in Eq. (11) dominates the interaction energy  $\Delta \mathcal{H}$ . In this case, the DDMMC algorithm randomly picks a charge, and then randomly picks a direction in which to move it. The move will be accepted only if it lowers the energy, i.e., if the charge advances in the direction of  $\mathbf{F}$ . This will happen only for a certain fraction  $p$  of the possible directions. For a triangular grid, with  $\mathbf{F}$  aligned with one of the grid basis vectors, three of the six possible nearest-neighbor directions will have a component parallel to  $\mathbf{F}$  and so  $p=1/2$ ; for a square grid,  $p=1/4$ . Thus, after one pass through the system, a randomly selected fraction  $p$  of the charges have advanced forward, while the rest remain in place. After a second pass through the system, a different randomly selected fraction  $p$  move forward. After many such passes one expects the system to be disordered. In fact, we find from simulations that, at  $T=0$ , DDMMC disorders the ground-state charge lattice for *all*  $F > F_c$ . The randomness of choosing moves, inherent in the DDMMC algorithm, is sufficient to disorder the moving system even as  $T \rightarrow 0$ .

We now consider the low- $T$  behavior of CTMC. For specificity we will consider the case of a triangular grid with a charge density of  $f=1/25$ , and  $\mathbf{F}=F\hat{a}_1$  aligned along one of the grid axes. We will study this particular case in great detail in Sec. III. Consider the limit  $T \rightarrow 0$ , starting in the  $F=0$  ground state and then increasing  $F$ , but with  $F < F_c$ . The configuration of charges in the  $F=0$  ground state is shown in Fig. 2(a) for a  $25 \times 25$  grid. Since CTMC is a rejectionless

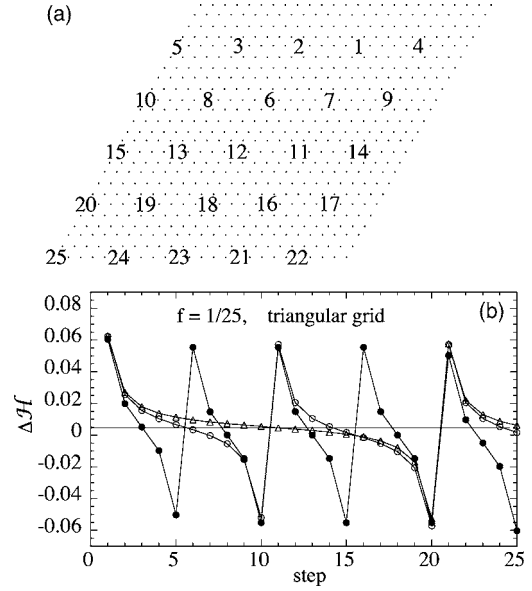


FIG. 2. CTMC on a triangular grid with charge density  $f = 1/25$  at  $T \rightarrow 0$  and  $F > F_c$ , with  $\mathbf{F}$  parallel to the  $\hat{a}_1$  axis. (a) Ground-state charge lattice for a  $25 \times 25$  triangular grid. Numbers denote the locations of the charges in the ground state. The value of each number indicates the step on which that charge moves forward. (b) The change in interaction energy  $\Delta \mathcal{H}$  at each step as charges move forward.  $\bullet$  are for a  $25 \times 25$  grid and correspond to the moves in (a);  $\circ$  and  $\triangle$  are the beginnings of similar sequences for  $50 \times 50$  and  $100 \times 100$  grids.

algorithm, even when  $F < F_c$  CTMC will make an excitation out of the ground state. However since  $\Delta U > 0$  for this excitation, the time  $\Delta t$  for this excitation to occur diverges exponentially as  $T \rightarrow 0$ . Conversely, once an excitation has been made, the very next move will be to relax the excitation back to the ground state, since this is the only move for which  $\Delta U < 0$ ; moreover, since  $\Delta U < 0$ , this move takes place in an exponentially vanishing time. Thus alternating steps of CTMC will consist of displacing a randomly selected single charge and then moving it back. As  $T \rightarrow 0$ , the simulation clock time to be in the ground state grows exponentially large, while the clock time to be in the excited state gets exponentially small. The system therefore remains pinned in the ground state, with the time in the excited states contributing negligibly to any measured averages.

Next, consider what happens when  $F > F_c$ . Because of the rates of Eq. (13), as  $T \rightarrow 0$  only moves with the smallest value of  $\Delta U_{i\alpha} \equiv \Delta U_{\min}$  can be selected; all other possible moves are exponentially suppressed. This results in the main difference between CTMC and DDMMC. In CTMC, as  $T \rightarrow 0$ , motion is deterministic except for choosing randomly among moves with degenerate values of  $\Delta U_{\min}$ . Now consider starting in the  $F=0$  ground state shown in Fig. 2(a). All moves that advance a charge forward one grid spacing along  $\hat{a}_1$  are equally likely, with  $\Delta U_{\min,1} = F_c - F < 0$ , while moves in all other directions are exponentially suppressed. Thus the first step will be to select any one of the  $N_c$  charges at random and move it forward. On the second step, however, there are only two moves that have the new lowest  $\Delta U_{\min,2}$ ; these are to advance either the charge immediately in front

of, or the charge immediately behind, the charge that moved in the first step. On the third step there are similarly only two moves with  $\Delta U_{\min,3}$ ; advancing the charge immediately in front of, or immediately behind, the first two moved charges. The system proceeds in a similar manner until all charges in the same row parallel to  $\mathbf{F}$  have moved forward. The next move will be to pick a charge at random in one of the two adjacent charge filled rows and move it forward, and then subsequently all charges in that row move forward one by one. In this manner, the rows of charges move one after another forward until the system has returned to the starting ground state, but with the entire charge lattice advanced by one grid spacing. In Fig. 2(a) we label each of the ground-state charges by the step number on which that charge moved forward in one particular pass of CTMC on a  $25 \times 25$  size grid. The pattern described above is clearly evident. In Fig. 2(b) we plot the change in interaction energy  $\Delta\mathcal{H} = \Delta U_{\min,n} + F$ , for each step  $n$  of this pass; note that  $\Delta\mathcal{H}$  is independent of the applied force  $F$ . The rough oscillation of  $\Delta\mathcal{H}$  with a period of  $n = L_1/a_0$ , with  $a_0 = 1/\sqrt{f}$  the spacing between the charges, reflects the row by row motion of the charges.

Next we consider the timing of the above sequence of moves. From Fig. 2(b) we conclude that for each step  $n > 1$  of the above pass  $U_{\min,n} < U_{\min,1}$ . Hence the rate (13) to make any step  $n > 1$  is exponentially larger than the rate to make the first step  $n = 1$ . As  $T \rightarrow 0$  we conclude that the relative time spent in the intermediate states (i.e., the states after steps  $n = 1, \dots, N_c - 1$ ) as compared to the time spent in the ordered ground state (prior to the first step and after step  $n = N_c$ ) vanishes exponentially. According to the simulation clock time, all charges in the ground-state charge lattice have advanced forward one grid spacing essentially simultaneously. This is the deterministic motion of the charge lattice that one would physically expect to find for  $F > F_c$  as  $T \rightarrow 0$ .

There is, however, one peculiar aspect to the above  $T \rightarrow 0$  dynamics. By the above arguments, the velocity of the moving charge lattice will be proportional to the rate to make the initial first step. From Eqs. (13) and (16) this rate will be  $W_{\text{tot}} = N_c W_0 e^{-\Delta U_{\min,1}/2T}$ . Thus the  $T \rightarrow 0$  velocity grows proportional to the number of charges  $N_c$  in the system. However, this can be understood physically if one views motion on the discrete grid as being a representation for continuum motion in a periodic potential. In this case, one should take  $W_0 \sim e^{-2U_0/T}$ , as in Eq. (22), where  $2U_0$  is the maximum to minimum energy difference of the potential. In the term  $W_{\text{tot}}$  above, the factor  $W_0$  represents the rate for a particular charge to be excited out of the ground state, over the energy barrier  $2U_0$  into the neighboring down stream potential minimum, thus lowering the energy of the system by  $\Delta U_{\min,1}$ . This rate becomes exponentially slow as  $T \rightarrow 0$ . Once this initial excitation has taken place, all the other charges follow, advancing forward in what may be regarded as an ‘‘avalanche.’’ We call this an avalanche because all the other charges move forward in a time that becomes vanishingly small compared to the time to make the initial excitation. The factor  $N_c$  in  $W_{\text{tot}}$  just reflects the  $N_c$  possible sites at which the initial excitation that leads to the avalanche can occur. Thus, while  $W_{\text{tot}}$  grows as  $N_c$ , it also vanishes exponentially as  $T \rightarrow 0$ , and so at  $T = 0$  the charges are always

pinned, as is physically appropriate for  $F_c < F < U_0$ .

Several features of the expected behavior at *finite*  $T$  can also be inferred from Fig. 2(b). Once a first charge in a given row has moved forward, the energy change for the other charges in the same row to move forward rapidly decreases. Consequently, once the first charge has moved forward, the remaining charges in that row rapidly follow forward. However, once a row has completely moved forward, the energy for the first charge in an adjacent row to move forward is not much lower than the energy for a first charge in any other row to move forward. Comparing the values of  $\Delta\mathcal{H}$  in Fig. 2(b) for steps  $n = 1$  and  $n = (L_1/a_0) + 1$ , we estimate this energy difference as  $\Delta E \approx 0.008$ . We therefore expect that once the temperature  $T$  becomes of the same order as this  $\Delta E$ , coherence between moving rows will be lost. Avalanches will now consist of individual rows moving forward, but different rows will be uncorrelated. Consequently, the average velocity in this regime will scale proportionally to  $L_1/a_0$  (the number of sites in a given row for an initial excitation to occur) rather than  $N_c$ . The details of this picture will depend on the specific correlations between charges within a given row, versus between rows, and this will be a subject of investigation in Sec. III.

### C. Observables

To determine the properties of our nonequilibrium steady states, we measure several static (time-independent) and dynamic (time-dependent) quantities. To determine structural properties, the main quantity of interest is the structure function

$$S(\mathbf{k}) \equiv \frac{1}{N_c} \langle n_{\mathbf{k}} n_{-\mathbf{k}} \rangle, \quad (23)$$

where

$$n_{\mathbf{k}} = \sum_i e^{i\mathbf{k} \cdot \mathbf{r}_i} n_i, \quad (24)$$

is the Fourier transform of the charge distribution  $n_i$ , and  $\mathbf{k}$  is one of the allowed wave vectors in the first Brillouin zone [shown in Fig. 1(b) for the triangular grid]. The corresponding real space correlation function is given by

$$C(m_1, m_2) \equiv \frac{1}{N} \sum_{k_1, k_2} e^{-2\pi i(m_1 k_1 + m_2 k_2)} S(k_1, k_2), \quad (25)$$

where we have expressed the positions  $\mathbf{r}_i$  and wave vectors  $\mathbf{k}$  in terms of their coordinates  $m_\mu$  and  $k_\mu$ , as in Eqs. (5) and (7), in constructing the above Fourier transform. We will also consider the mixed correlation

$$C(k_1, m_2) \equiv \frac{1}{N} \sum_{k_2} e^{-2\pi i m_2 k_2} S(k_1, k_2). \quad (26)$$

The above quantities give information about the translational order of the system. To investigate the orientational order, we define the six-fold orientational (hexatic) order parameter

$$\Phi_6 \equiv \frac{1}{N_c} \sum_i \frac{1}{z_i} \sum_j e^{\delta i \theta_{ij}}. \quad (27)$$

In the above, the first sum is over all charges  $n_i=1$ , the second sum is over all charges  $n_j=1$  that are nearest neighbors of  $n_i$ ,  $z_i$  is the number of such nearest neighbors, and  $\theta_{ij}$  is the angle of the bond from  $n_i$  to  $n_j$  with respect to the  $\hat{a}_1$  axis. Nearest neighbors are determined by Delaunay triangulation.<sup>12</sup>

We also measure several dynamical quantities. Let

$$\mathbf{R}_{\text{c.m.}}(t) \equiv \frac{1}{N_{c,s < t}} \sum \Delta \mathbf{r}_s \quad (28)$$

be the net displacement of the center of mass of the charges at time  $t$  of the simulation clock. The right-hand side of the above is just the sum of charge displacements at each step  $s$  of the simulation that occurs before the simulation clock has reached time  $t$ , normalized by the total number of charges. The average velocity of the system is then just

$$\mathbf{v}_{\text{ave}} = \frac{\mathbf{R}_{\text{c.m.}}(\tau) - \mathbf{R}_{\text{c.m.}}(t_{\text{eq}})}{\tau - t_{\text{eq}}}, \quad (29)$$

where  $\tau$  is the total simulation clock time and  $t_{\text{eq}}$  is some initial time to allow for equilibration. In the analogy between 2D charges and vortices in a superconducting film, the average charge velocity becomes the average voltage drop transverse to the direction of motion of the vortices.

We also look at the fluctuations about the average center of mass position. If we define the fluctuation, after a time  $t$ , about the average center-of-mass position

$$\delta \mathbf{R}(t; t_0) \equiv \mathbf{R}_{\text{c.m.}}(t + t_0) - \mathbf{R}_{\text{c.m.}}(t_0) - \mathbf{v}_{\text{ave}} t, \quad (30)$$

then we can define the diffusion tensor  $\mathbf{D}(t)$  by

$$2\mathbf{D}(t) \equiv N_c \langle \delta \mathbf{R}(t; t_0) \delta \mathbf{R}(t; t_0) \rangle_{t_0}, \quad (31)$$

where the angular brackets in the above denote an average over the parameter  $t_0$  during the course of a single simulation. In averaging over  $t_0$ , we restrict ourselves to nonoverlapping intervals, i.e., to the values  $t_0=nt$ , for integer  $n$ , so as to reduce correlations among the different terms being averaged. If fluctuations about the center of mass are diffusive, then we expect  $\mathbf{D}(t)$  to saturate to a constant as  $t$  increases. The factor  $N_c$  on the right-hand side of Eq. (31) ensures that  $\mathbf{D}(t)$  approaches a size-independent value in the liquid state, where the charges have only short ranged correlations.

Although in our simulation we will use Eq. (31) to compute  $\mathbf{D}(t)$ , the diffusion tensor can also be expressed in its more familiar form, in terms of velocity correlations.<sup>13</sup> If we define the instantaneous fluctuation in velocity by

$$\delta \mathbf{v}(t) \equiv \mathbf{v}(t) - \mathbf{v}_{\text{ave}} = \delta \mathbf{R}(\Delta t; t) / \Delta t, \quad (32)$$

then

$$\lim_{t \rightarrow \infty} \mathbf{D}(t) = \frac{N_c}{2} \int_{-\infty}^{\infty} dt \langle \delta \mathbf{v}(t) \delta \mathbf{v}(0) \rangle. \quad (33)$$

For a superconducting network, where vortex velocity is proportional to the voltage drop in the direction transverse to the

vortex motion,  $\mathbf{D}$  is a measure of the voltage fluctuations.

In equilibrium, when  $\mathbf{F}=\mathbf{v}_{\text{ave}}=0$ ,  $\mathbf{D}/T$  is proportional to the charge mobility tensor by the fluctuation-dissipation theorem.<sup>14</sup> In the analogy to vortices in superconducting films, this is the linear resistivity of the film. In the driven state, with  $\mathbf{F}=F\hat{x}$ , we will use the transverse component of the diffusion tensor  $D_{yy}$  to test for the presence of transverse pinning. If  $D_{yy}>0$ , the center-of-mass is diffusing transversely to the direction of the average motion; application of a small transverse force  $\delta F\hat{y}$  will cause the system to acquire a transverse component of the velocity  $v_y \propto \delta F$ . In analogy with equilibrium, we will assume that if  $D_{yy}=0$ , there will be no linear transverse response, i.e.,  $v_y/\delta F \rightarrow 0$  as  $\delta F \rightarrow 0$ . This characterizes a transversely pinned state.<sup>15</sup>

In CTMC, averages in the steady state are computed by the time integral in Eq. (17). However, the direct application of Eq. (17) would require the evaluation of the measured quantity after *every* single step of the simulation. For quantities involving lengthy calculation, such as  $S(\mathbf{k})$  and  $\Phi_6$ , this is not practical except for fairly short runs. Instead, we compute the time integrals for these quantities by a Monte Carlo integration,<sup>16</sup> averaging them over  $N_{\text{config}}$  configurations sampled randomly, with a uniform distribution, over the simulation clock time interval  $(t_{\text{eq}}, \tau)$ , with  $t_{\text{eq}}$  an initial equilibration time and  $\tau$  the total simulation time. In practice, we implement this scheme as follows. We compute the average time interval between samplings  $\tau' = (\tau - t_{\text{eq}}) / N_{\text{config}}$ . Then, after a first sampling, we determine the time until the next sampling by drawing from an exponential distribution with average time constant  $\tau'$ . This gives the correct sampling since, if  $t_1 < t_2 \dots < t_n$  are the ordered values of  $n$  independent and uniformly distributed random variables on a given interval, the probability distribution for the distance  $t_{i+1} - t_i$  is exponential. We use typically  $N_{\text{config}} \approx 10^3$  to  $10^4$  in our simulations.

### III. RESULTS ON A TRIANGULAR GRID

We now report our results for the case of charges on a triangular grid. The equilibrium, i.e.,  $\mathbf{F}=0$ , behavior<sup>6</sup> of this system depends on the charge density  $f$ . For sufficiently dense  $f$  (but not too dense), there is only a single first order melting transition at  $T_m$ , from a pinned charge solid with long range translational order at low  $T$ , to an ordinary liquid at high  $T$ . For more dilute  $f$ , there are three phases: a low- $T$  pinned solid with long-range translational order, an intermediate- $T$  floating solid with algebraic translational order, and a high- $T$  liquid. In this work we will consider the charge density  $f=1/25$ , which falls in the dense limit with a single first order equilibrium melting temperature of  $T_m \approx 0.0085$ . The dilute limit will be considered elsewhere.

#### A. Phase diagram

We start by mapping out the  $T$ - $F$  phase diagram for a  $60 \times 60$  grid, with the applied force along the  $\hat{a}_1$  grid axis,  $\mathbf{F}=F\hat{x}$ . We initialize the system in the ordered  $F=0$  ground state, set  $F$  to the desired driving force, and then simulate the system for increasing values of  $T$ . By measuring the average



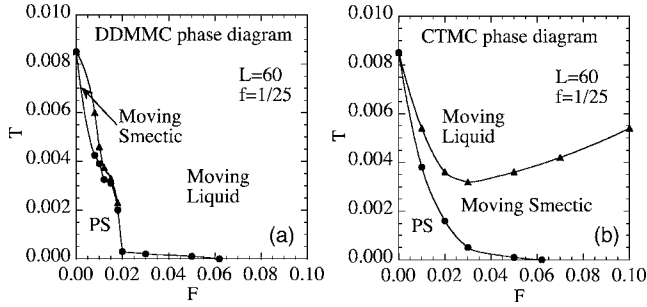


FIG. 3. Phase diagram for a  $60 \times 60$  triangular grid with charge density  $f=1/25$  as a function of temperature  $T$  and driving force  $\mathbf{F}=F\hat{x}$ , (a) for DDMMC dynamics and (b) for CTMC dynamics. “PS” stands for pinned solid.

interaction energy  $\langle \mathcal{H} \rangle$ , structural properties such as  $S(\mathbf{k})$  and  $\langle \Phi_6 \rangle$ , and the average velocity  $\mathbf{v}_{\text{ave}}$ , we determine the phase diagrams shown in Fig. 3. Our simulations consist typically of  $\sim 10^5 - 10^6$  passes through the system, depending on system size and parameters.

Our results for the DDMMC dynamics are shown in Fig. 3(a). As discussed earlier in Sec. II B 3, at  $T=0$  the system remains pinned ( $\mathbf{v}_{\text{ave}}=0$ ) in its equilibrium ground state for all  $F$  below a critical force  $F_c=0.0603$ ; for all  $F > F_c$  the moving state is a liquid.<sup>8</sup> For fixed  $F < F_c$ , upon increasing  $T$ , the solid remains pinned with long range translational order, up until a value  $T_p(F)$ . It then enters a moving state with finite  $\mathbf{v}_{\text{ave}}$ . Over most of the phase diagram we find<sup>8</sup> that this moving state is a liquid with a correlation length of order the spacing between charges  $a_0$ . Only in a very narrow region at low  $F$  and higher  $T$  do we find a structure that appears to be a moving smectic. We will discuss what we mean by a “smectic” phase in greater detail when we describe our results from CTMC. For DDMMC we have not investigated in any detail the stability of this small region of smectic phase

with respect to increasing the system size, or with respect to cooling from the liquid. The lack of structure for almost all of the moving state, particularly at large  $F$  and small  $T$ , suggests that the DDMMC algorithm is indeed unphysical and unlikely to be a good model for continuum dynamics. We therefore focus on the CTMC algorithm for the remainder of this paper.

In Fig. 3(b) we give the phase diagram for CTMC dynamics. Again we find pinned, liquid, and smectic phases, but now the smectic persists over a wide region of the  $T$ - $F$  plane, particularly at low  $T$  and large  $F$ . To illustrate the nature of order in each of these phases, we plot in Fig. 4 the structure function  $S(\mathbf{k})$  for several representative points in the phase diagram. In Fig. 4(a) we see the sharp Bragg peaks with  $S(\mathbf{K}) \approx N_c$ , characteristic of the long-range translational order in the pinned solid phase. The peaks are at the reciprocal lattice vectors of the ordered charge solid, and given by

$$\mathbf{K}_{p_1, p_2} = k_1 \mathbf{b}_1 + k_2 \mathbf{b}_2$$

with

$$k_\mu = \frac{p_\mu}{5}, \quad p_\mu = 0, \pm 1, \pm 2. \quad (34)$$

Figure 4(b) shows a roughly circular and finite peak, characteristic of short-range translational order in the moving liquid phase.

Figures 4(c) and 4(d) show the moving smectic at small and large driving forces, respectively. Consider first the large drive case in Fig. 4(d). The peaks along the  $k_2$  axis ( $k_1=0$ ) at  $(k_1, k_2) = (0, \pm 1/5)$  and  $(0, \pm 2/5)$  [see Fig. 1(b) for the  $k$ -space geometry] are sharp Bragg peaks with  $S(\mathbf{K}) \approx N_c$ . This indicates that if one averages the particle density in the  $\hat{a}_1$  direction ( $k_1=0$ ), the resulting density is periodic in the  $\hat{a}_2$  direction with a period of five grid spacings; the particles are therefore moving in periodically spaced channels oriented

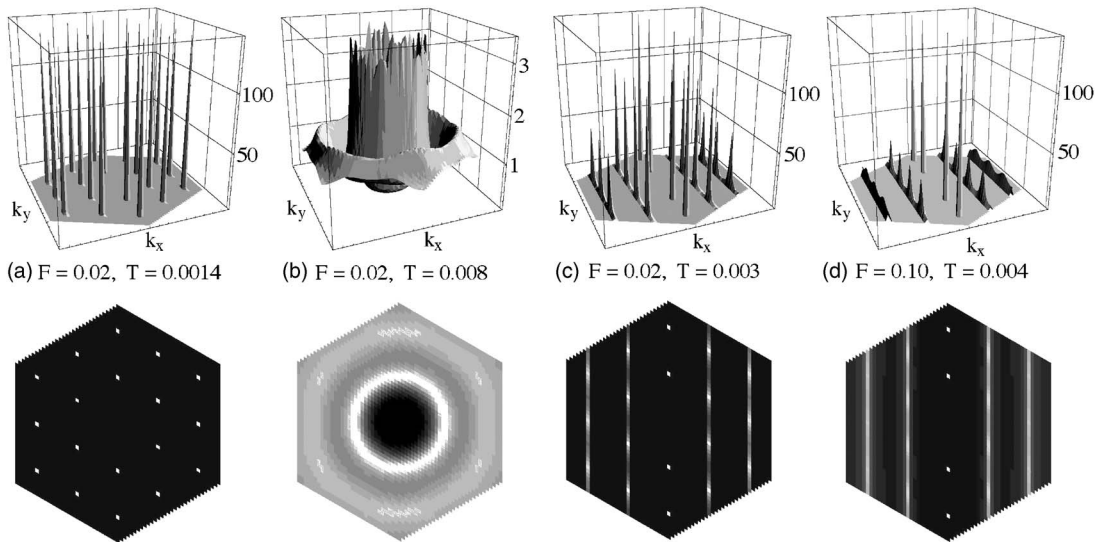


FIG. 4.  $S(\mathbf{k})$  for several points in the CTMC phase diagram of Fig. 3(b). (a)  $F=0.02$ ,  $T=0.0014$  in the pinned solid; (b)  $F=0.02$ ,  $T=0.008$  in the moving liquid; (c)  $F=0.02$ ,  $T=0.003$  in the moving smectic; (d)  $F=0.10$ ,  $T=0.004$  in the moving smectic at higher drive. The bottom row shows intensity plots of the corresponding graphs in the top row. The peak  $S(\mathbf{k}=0) = N_c$  is removed to give greater contrast to the other peaks.



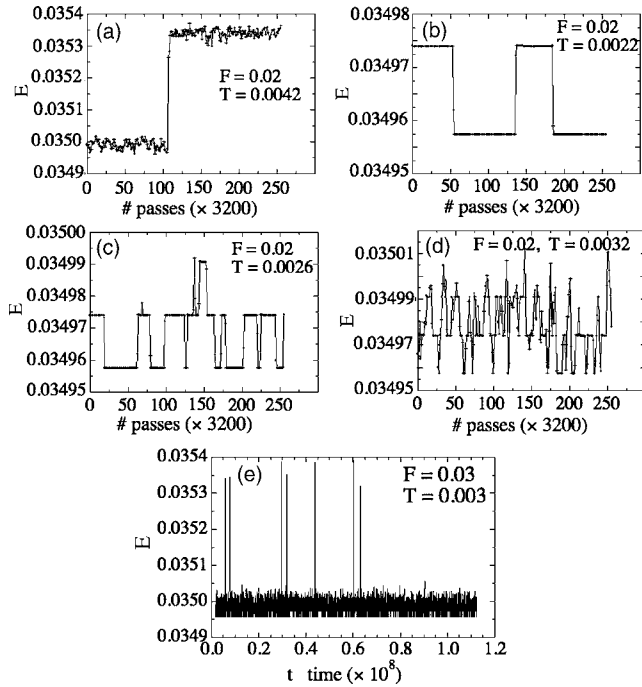


FIG. 5. (a)–(d) Average interaction energy per site  $E=\langle\mathcal{H}/N\rangle$  vs the number of simulation passes through the grid. Each point represents an average over 3200 successive passes; (a)  $F=0.02$ ,  $T=0.0042$ , just at the melting transition  $T_m(F)$ ; (b)  $F=0.02$ ,  $T=0.0022$ , just above the unpinning transition  $T_p(F)$ ; (c)  $F=0.02$ ,  $T=0.0026$ ; and (d)  $F=0.02$ ,  $T=0.0032$ , moving away from the unpinning transition. (e)  $E$  vs simulation clock time  $t$ , for  $F=0.03$ ,  $T=0.003$ , slightly below the melting transition.

parallel to the driving force  $\mathbf{F}=F\hat{a}_1$ . Next, note that the peaks at finite  $k_1=\pm 1/5, \pm 2/5$  appear to be sharp, i.e., only one grid spacing wide, along the  $k_1$  direction. Such  $\delta$ -function-like peaks in the  $k_1$  direction indicate that the particles are periodically ordered within each smectic channel with a period of five grid spacings. The finite width of these peaks in the  $k_2$  direction indicates that the ordered smectic channels are randomly displaced with respect to each other, with a finite correlation length  $\xi_\perp$  proportional to the inverse width of the peak. Comparing Fig. 4(c) with 4(d), we see similar features at the smaller drive  $F$ , only the peaks at finite  $k_1$  are now sharper, with a narrower width in the  $k_2$  direction. In the next two sections we will consider these features of the smectic phase in much greater detail, studying the scaling behavior and stability of the smectic as the system size increases.

Finally we consider the nature of the melting transition  $T_m(F)$  from the smectic to the liquid, and the unpinning transition  $T_p(F)$  from the pinned solid to the smectic. In Figs. 5(a)–5(d) we plot the average interaction energy per site,  $E=\langle\mathcal{H}/N\rangle$  vs. the number of simulation passes through the grid. Each point represents an average over 3200 successive passes. Figure 5(a) shows results at  $F=0.02$ ,  $T=0.0042$ , just at the melting transition  $T_m(F)$ . We see that the energy takes a discontinuous jump as the system makes the transition from smectic to liquid. Melting of the smectic is therefore like a first order phase transition. Figure 5(b), shows results

at  $F=0.02$ ,  $T=0.0022$ , just above the unpinning transition  $T_p(F)$ . We see that the energy fluctuations form a set of plateaus, with a very long period of fluctuation. The lowest plateau corresponds to the ordered  $F=0$  ground state with a value  $E_0=0.03495736$ . The higher-energy plateau corresponds to having some fraction of adjacent smectic channels (i.e., charge filled rows) advanced one grid spacing parallel to  $\mathbf{F}$ , so that the system looks locally similar to the ground state, but with one pair of domain walls parallel to  $\mathbf{F}$ .

As  $T$  increases above  $T_p$ , Figs. 5(c) and 5(d) show that the rate of fluctuations increase, and plateaus of additional energy values appear. The higher-energy plateaus correspond to having more than one pair of domain walls in the otherwise ordered system. This behavior may be understood by considering the results shown in Fig. 2(b). For a driving force of  $F=0.02$ , the thermal energy needed to excite a pair of adjacent particles in a given row to move forward is  $\Delta U=\Delta U_{\min,1}+\Delta U_{\min,2}\approx 0.048$ ; however, the energy to move each remaining particle is  $\Delta U_{\min,n}<0$ . Thus, at low  $T$ , the excitation of an initial pair forward will trigger the remaining particles in that row to move forward almost instantaneously. The rate for the initial pair excitation goes as  $W\sim e^{-\Delta U/2T}$  vanishing exponentially as  $T$  decreases. The rate of energy fluctuations decreases accordingly. At low  $T$ , once a given row has moved forward, the next most favorable excitation is to move an adjacent row of charges forward (see discussion at the end of Sec. II B 3). The system thus consists of a single pair of domain walls in the otherwise ordered ground state; the distance between the domain walls increases as more adjacent rows move forward. Such states give the higher of the two energy plateaus in Fig. 5(b). As  $T$  increases, there becomes a non-negligible probability to have a pair excitation in a nonadjacent row of charges. Now the system can develop more than a single pair of domain walls, leading to the additional high energy plateaus of Figs. 5(c) and 5(d).

The above arguments suggest that  $T_p(F)$  may not be a true phase transition. Since the above rate  $W$  is finite at any  $T$ , but grows vanishingly small as  $T\rightarrow 0$ , the observed  $T_p(F)$  may just result from  $1/W$  growing larger than the longest simulation time we can carry out. As  $F$  decreases, it will become necessary to excite three, then four, then more, particles forward in a given row, before one reaches the condition that  $\Delta U_{\min,n}<0$  triggering the remaining particles in the row to move immediately forward [see Fig. 2(b)]. Thus we expect that  $W$  will decrease, and the observed  $T_p(F)$  will increase, as  $F\rightarrow 0$ . Note that the graphs in Figs. 5(a)–5(d) are plotted versus the number of simulation passes rather than the simulation clock time. They therefore reflect the amount of actual computation needed to observe fluctuations of the system. The decrease in fluctuation rate observed as  $T$  decreases for fixed  $F=0.02$  [compare Fig. 5(d) to 5(b)] results from the decrease in probability to move the second particle of an excitation pair forward, *before* the first particle has had a chance to fall back into place, rather than being directly due to the overall exponential decrease with  $T$  of all single particle rates as in Eq. (13).

Finally we note that, for finite system size, the moving smectic state is the true stable steady state of the system. In Fig. 5(e) we plot the average interaction energy per site  $E$

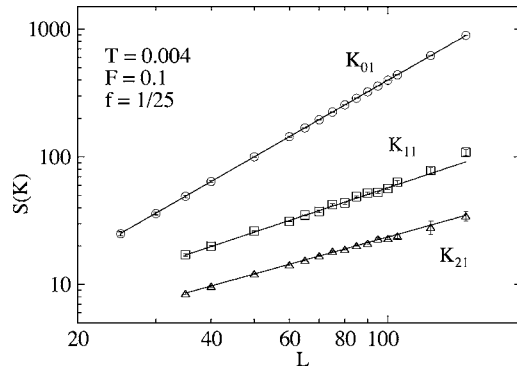


FIG. 6. Scaling of peak heights  $S(\mathbf{K})$  vs system size  $L$  for the smectic phase at  $F=0.10$ ,  $T=0.004$ . Straight lines indicate good power law fits,  $S(\mathbf{K}) \sim L^s$ , with  $s \approx 1.99$  for  $\mathbf{K}_{01}$ ,  $s \approx 1.15$  for  $\mathbf{K}_{11}$ , and  $s \approx 0.96$  for  $\mathbf{K}_{21}$ .

versus simulation clock time  $t$ , for the parameters  $F=0.03$ ,  $T=0.003$ , which lies just immediately below the melting transition  $T_m(F)$  [see Fig. 3(b)]. Comparing with Fig. 5(a), we see clearly that the system has occasional fluctuations into the liquid phase, as indicated by the large brief spikes in energy. Such fluctuations are expected for a finite size system near a first-order phase transition. The fact that the system returns to the smectic state, after such a liquid fluctuation, indicates that the smectic is indeed the stable steady state. We have also succeeded in cooling into the smectic state from the disordered liquid, and in entering the smectic from the liquid by increasing  $F$  at temperatures above the minimum of the  $T_m(F)$  transition boundary.

### B. Smectic phase—High drive

In the next two sections we explore in detail the nature of ordering in the moving smectic state, and its stability as the system size increases. We start here by considering the smectic in the high drive case at  $F=0.1$ ,  $T=0.004$ , corresponding to Fig. 4(d). If the system has true long-range smectic order, we expect the peaks in  $S(\mathbf{k})$  along the  $k_2$  axis ( $k_1=0$ ) to be true Bragg peaks, with a height that scales as the system area. In Fig. 6 we plot the height of the peak  $S(\mathbf{K}_{01})$ , versus system length  $L$ , for systems of size  $L \times L$ . The straight line on the log-log plot has a slope  $s \approx 1.99$  giving good agreement with the  $\sim L^2$  behavior expected for long-range smectic order.

Next we consider the ordering within the smectic channels. If charges have long-range order within each individual channel, we expect the peaks in  $S(\mathbf{k})$  at  $k_1 = \pm 1/5, \pm 2/5$  to be  $\delta$ -function-like in the  $k_1$  direction. If the channels have only short-range correlations between them, the width of these peaks will remain finite in the  $k_2$  direction. We therefore expect that the heights of these peaks at finite  $k_1$  should scale as the system length  $L_1$  in the  $\hat{a}_1$  direction. In Fig. 6 we plot the height of two of these peaks  $S(\mathbf{K}_{11})$  and  $S(\mathbf{K}_{21})$  [see Eq. (34) for our notation labeling the reciprocal lattice vectors  $\mathbf{K}$ ] versus system length  $L$ , for systems of size  $L \times L$ . The straight lines have slopes  $s=1.15$  and  $0.96$  respectively, in reasonable agreement with the  $\sim L$  behavior described above.

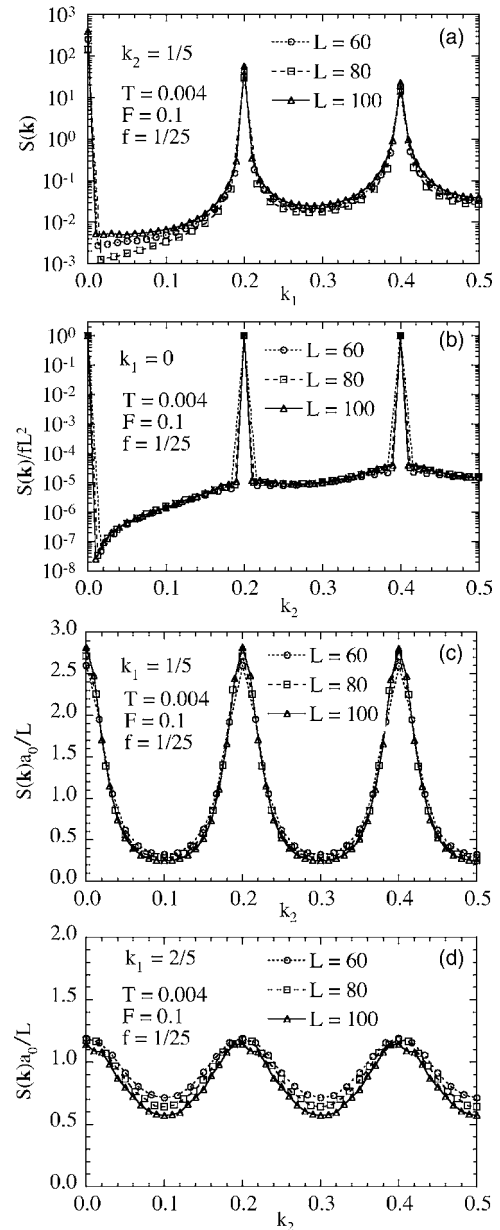


FIG. 7. Profiles of  $S(\mathbf{k})$  in various directions, for different system sizes  $L$ , for the smectic phase at  $F=0.10$ ,  $T=0.004$ . (a)  $S(\mathbf{k})$  vs  $k_1$  for fixed  $k_2=1/5$ ; (b)  $S(\mathbf{k})/fL^2$  vs  $k_2$  for fixed  $k_1=0$ ; (c)  $S(\mathbf{k})a_0/L$  vs  $k_2$  for fixed  $k_1=1/5$ ; (d)  $S(\mathbf{k})a_0/L$  vs  $k_2$  for fixed  $k_1=2/5$ . Note the logarithmic scale in (a) and (b).

To further illustrate the above results, we plot in Fig. 7 profiles of  $S(\mathbf{k})$  along different paths through the first Brillouin zone, for various  $L \times L$  system sizes. Figure 7(a) shows  $S(\mathbf{k})$  vs  $k_1$  for fixed  $k_2=1/5$ . The logarithmic vertical scale, varying over five orders of magnitude, indicates how sharply the peaks are confined to the values  $k_1=1/5, 2/5$ ; however,  $S(\mathbf{k})$  appears to decrease continuously as one moves away from the peak values. Figure 7(b) shows the peaks indicating the smectic order, i.e.,  $S(\mathbf{k})/fL^2$  versus  $k_2$  for fixed  $k_1=0$ . We see that the peaks, scaled by  $N_c=fL^2$ , all have the same height for the different  $L$ , in agreement with the scaling seen in Fig. 6. The logarithmic vertical scale, dropping five orders

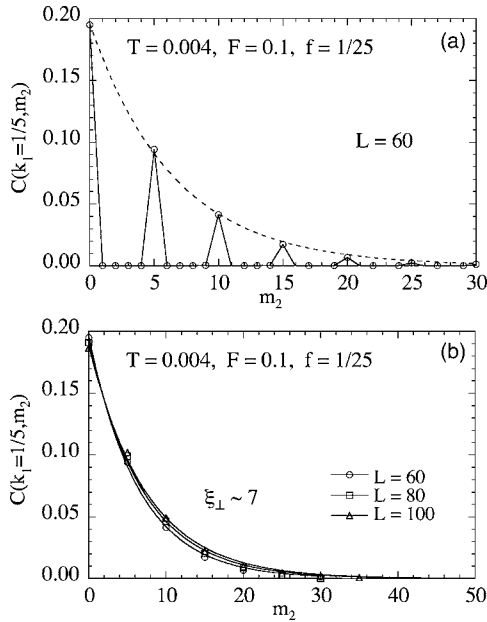


FIG. 8. Transverse correlation function  $C(k_1=1/5, m_2)$  vs  $m_2$  at  $F=0.1$ ,  $T=0.004$ . (a)  $C(k_1=1/5, m_2)$  for all integer values  $m_2$  for the single size  $L=60$ ; the dashed line highlights the decaying envelope of the peaks, while the solid line interpolates between the data points. (b) Peak values of  $C(k_1=1/5, m_2)$  at values  $m_2=5n$ ,  $n$  integer, for different sizes  $L$ ; solid lines are fits to the periodic exponential of Eq. (35).

of magnitude as one moves a single grid point in  $k$  space away from the peaks at  $k_2=1/5$ ,  $2/5$ , shows that these are indeed sharp Bragg peaks. In Figs. 7(c) and 7(d) we show the peaks at finite  $k_1$ , plotting  $S(\mathbf{k})a_0/L$  versus  $k_2$  for fixed  $k_1=1/5$  and  $k_1=2/5$ , respectively. We see that these profiles, when scaled by  $1/L$ , collapse reasonably well to a common curve for the different sizes  $L$ , for all values of  $k_2$ . This is in agreement with the scaling found in Fig. 6, and suggests that  $S(\mathbf{k})$  is indeed  $\delta$ -function-like in  $k_1=1/5$ ,  $2/5$  for all  $k_2$ .

The finite widths in the  $k_2$  direction of the peaks in  $S(\mathbf{k})$  at  $k_1=1/5$ ,  $2/5$ , which do not narrow as  $L$  increases, indicate that the ordered smectic channels have only short-range correlations between them. To see this explicitly, consider the Fourier transform of the charge density in each row of the grid at the wave vector corresponding to the periodic ordering within the smectic channels, i.e.,  $\mathbf{k}=(1/5)\mathbf{b}_1$ , and compute the correlations of this Fourier amplitude between different rows. This is given by the correlation function  $C(k_1=1/5, m_2)$ , defined in Eq. (26). In Fig. 8(a) we plot  $C(k_1=1/5, m_2)$  versus  $m_2$  for a  $60 \times 60$  system. The correlation has peaks at values  $m_2=5n$ ,  $n$  integer, and is essentially zero in between, indicating that the particles flow in periodically spaced channels, and that the channels have a width of a single grid spacing. The exponential decay of the peak heights indicates the short range correlation between particles in different smectic channels. In Fig. 8(b) we plot only the peaks of  $C(k_1=1/5, m_2)$ , but for different system sizes  $L \times L$ . The curves for different  $L$  lie almost on top of each other and decay to zero, indicating a finite, size independent, correlation length  $\xi_\perp$  transverse to the direction of the ap-

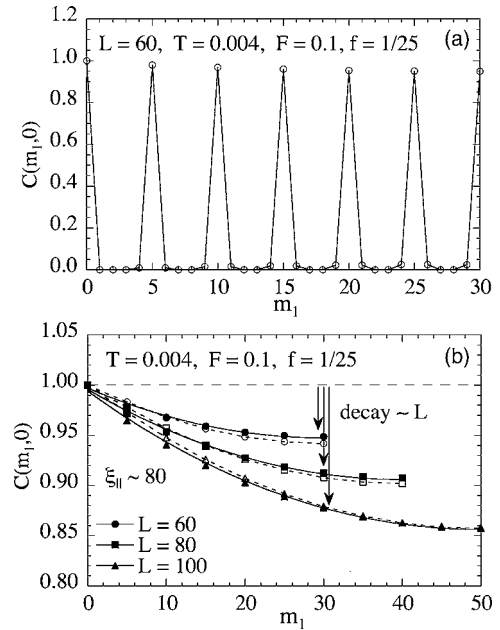


FIG. 9. Longitudinal correlation function  $C(m_1, m_2=0)$  vs  $m_1$  at  $F=0.1$ ,  $T=0.004$ . (a)  $C(m_1, 0)$  for all integer values  $m_1$  for the single size  $L=60$ . (b) Peak values of  $C(m_1, 0)$  at values  $m_1=5n$ ,  $n$  integer, for different sizes  $L$  (solid symbols); solid lines are fits to the periodic exponential of Eq. (36). Open symbols and dashed lines are fits to a one-dimensional model (see text).

plied force  $\mathbf{F}$ . To estimate  $\xi_\perp$  we fit to a simple periodic exponential

$$C(k_1=1/5, m_2) \approx A(e^{-m_2/\xi_\perp} + e^{-(L-m_2)/\xi_\perp}), \quad (35)$$

and get values in the range  $\xi_\perp \approx 7.0 \pm 0.5$  as  $L$  varies from 60 to 100. Thus correlations extend only slightly beyond nearest neighbor channels (which are separated by five grid spacings).

Next we compute the correlations within individual smectic channels. In Fig. 9(a) we plot the real space correlation parallel to the driving force  $C(m_1, m_2=0)$  versus  $m_1$ , for a system of size  $60 \times 60$ . Again we see sharply defined peaks at  $m_1=5n$ ,  $n$  integer, corresponding to the periodic spacing of particles within the channel. Moreover the height of these peaks decays only slightly to a large finite value as  $m_1 \rightarrow L/2$ , as one would expect for long-range order. However, when we plot in Fig. 9(b) the height of these peaks for different values of  $L$  for system sizes  $L \times L$ , we now see behavior inconsistent with long-range order. The value of  $C(m_1, 0)$  at any given value of  $m_1$  decreases as  $L$  increases; the magnitude of this decrease from unity is proportional to  $L$ . Rather than indicating long-range order, such behavior is consistent with a very dilute but finite density of order destroying defects; when  $L$  is small compared to the average spacing between defects, then the probability to have a defect in the system will be proportional to  $L$ , resulting in a decrease in the correlation proportional to  $L$ .

Indeed, since the smectic channels are essentially decoupled from each other (as illustrated in Fig. 8), each channel can be thought of as an independent one-dimensional system.

Although the charges in the channel have a bare long-range logarithmic interaction, the uncorrelated motion of charges in neighboring smectic channels will screen this log interaction, converting it to an effective interaction that is finite ranged. To test this picture we perform independent CTMC simulations of a one-dimensional (1D) lattice gas of particles with average spacing 5 and a nearest-neighbor harmonic interaction with a spring constant  $\kappa$ . Carrying out simulations for the same system sizes  $L$  as in Fig. 9(b), we adjust  $\kappa$  to get the best fit to the correlations found in the original two dimensional system. This gives a reasonable value of  $\kappa=0.0505$ , and our 1D results are shown as the open symbols and dashed lines in Fig. 9(b). We see that the agreement is very good; the small deviations that exist are presumably due to the small but finite coupling between neighboring smectic channels that exists in the original 2D model. Having found  $\kappa$ , we can now simulate the 1D model for much larger  $L$ , to see the exponential decay of correlations in the model and to determine the correlation length  $\xi_{\parallel}$ . We find for the 1D model,  $\xi_{\parallel} \approx 86$ . For comparison, we can fit the data from the original 2D model to a periodic exponential

$$C(m_1, m_2 = 0) \approx c_1 + c_2(e^{-m_1/\xi_{\parallel}} + e^{-(L-m_1)/\xi_{\parallel}}), \quad (36)$$

where  $c_1=1/5$  is the average density of charges in a smectic channel, and  $c_2=4/5$  is chosen so that  $C(0,0)=1$ . The resulting fits are shown as the solid lines in Fig. 9(b), and give the values  $\xi_{\parallel} \approx 83, 80, 78$  for sizes  $L=60, 80, 100$ , in good agreement with the 1D model. We conclude that the smectic phase at high drive consists of weakly coupled channels, characterized by a small transverse correlation length  $\xi_{\perp}$ . Within each channel particles have only finite-range correlations, but, for the case considered above, this longitudinal correlation length is comparable to the size of the system,  $\xi_{\parallel} \geq L \gg \xi_{\perp}$ , so that the particles in a given channel appear to be ordered.

We can next ask what happens if the system length parallel to the driving force  $\mathbf{F}$  increases to be larger than the longitudinal correlation length  $L_1 > \xi_{\parallel}$ . Increasing the system to size  $L_1 \times L_2 = 500 \times 60$ , so that this condition is met, we found in Ref. 8 that the smectic phase at  $F=0.1$ ,  $T=0.004$ , becomes unstable to the liquid; for this system with bigger  $L_1$ , the smectic remains stable only at lower  $T$  such that the condition  $L_1 \leq \xi_{\parallel}$  is again obeyed. To illustrate this point further, we carry out simulations for a system of size  $60 \times 60$  at  $F=0.1$ , but increasing  $T$  so as to cross the melting line shown in the phase diagram of Fig. 3(b). In Fig. 10 we plot the resulting correlation functions  $C(m_1, m_2=0)$  versus  $m_1$  for several different temperatures. We see clearly the transition from smectic to liquid at a temperature between 0.005 and 0.006. To get an estimate of the longitudinal correlation length  $\xi_{\parallel}$  we fit the data of Fig. 10 to a periodic exponential, as in Eq. (36). For the smectic,  $T \leq 0.005$ , we set  $c_1=1/5$  as appropriate for the average density of charges in a smectic channel. For the liquid,  $T \geq 0.006$ , we set  $c_1=1/25$ , appropriate for the average density of charges in the liquid. Since the periodic exponential of Eq. (36), with a single decay length  $\xi_{\parallel}$ , only needs to describe behavior at large  $m_1$  (decay at small  $m_1$  possibly being described by additional, shorter, length scales), we consider fits in which we drop the data at some of the initial small values of  $m_1$ , and keep  $c_2$  as a free

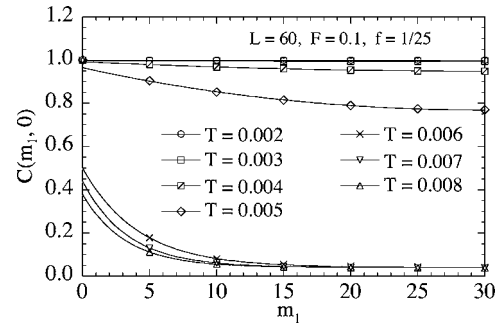


FIG. 10. Correlation function  $C(m_1, m_2=0)$  vs  $m_1$  at  $F=0.1$  and various  $T$ , for a  $60 \times 60$  system. Only the peak values at  $m_1=5n$ ,  $n$  integer, are shown. Solid lines are fits to an appropriate periodic exponential, as in Eq. (36), excluding the initial point at  $m_1=0$  from the fit.

fitting parameter. For both the smectic and the liquid we find the best fits to Eq. (36) when we exclude only the initial point at  $m_1=0$ ,  $C(0,0)=1$ , from the fit. The resulting fits are shown as the solid lines in Fig. 10. The values of  $\xi_{\parallel}$  obtained from these fits are then plotted versus  $1/T$  in Fig. 11(a). The dashed straight line on the plot indicates an Arrhenius form  $\xi_{\parallel} \sim e^{T_0/T}$  for the divergence of  $\xi_{\parallel}$  in the smectic as  $T \rightarrow 0$ . We see that melting occurs when  $\xi_{\parallel} \sim 30$ , i.e., roughly half the system length. We conclude that the smectic is only stable when  $\xi_{\parallel} \geq L/2$ . When the correlation length becomes smaller than this, and one would expect particles within the smectic channels to disorder, the entire smectic structure becomes unstable to a liquid. Since  $\xi_{\parallel}$  diverges rapidly as  $T \rightarrow 0$ , however, one should expect to see the smectic phase in any finite size system, at sufficiently low temperature.

Finally, we can also estimate the transverse correlation length  $\xi_{\perp}$ . For the smectic we use an analysis of  $C(k_1=1/5, m_2)$ , similar to that of Fig. 8(b), to determine  $\xi_{\perp}$ . For the liquid, since there is no periodic ordering, we use an analysis similar to that of Fig. 10 applied to the real space correlation  $C(x=0, y)=C(m_1=-m_2/2, m_2)$  versus  $y=(\sqrt{3}/2)m_2$ . Note that since the direction  $\hat{a}_2$  is not orthogonal to  $\hat{a}_1$  [see Fig. 1(a)] it is necessary to use the argument  $m_1=-m_2/2$  in order to measure a strictly transverse correlation. Our results for  $\xi_{\perp}$  versus  $T$  are shown in Fig. 11(b). Unlike the rapid rise in  $\xi_{\parallel}$  as  $T$  decreases, we see only a small in-

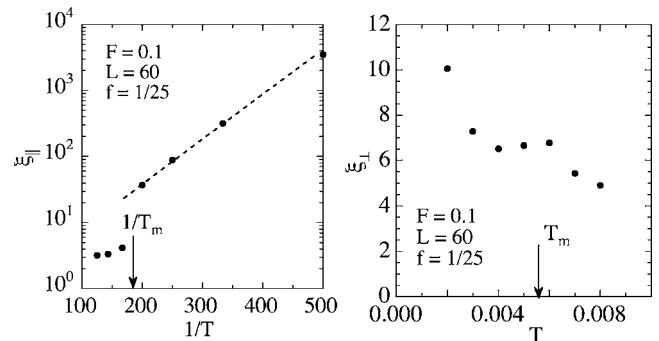


FIG. 11. (a) Longitudinal correlation length  $\xi_{\parallel}$  vs  $1/T$  and (b) transverse correlation length  $\xi_{\perp}$  vs  $T$ , at  $F=0.1$  for a  $60 \times 60$  system.



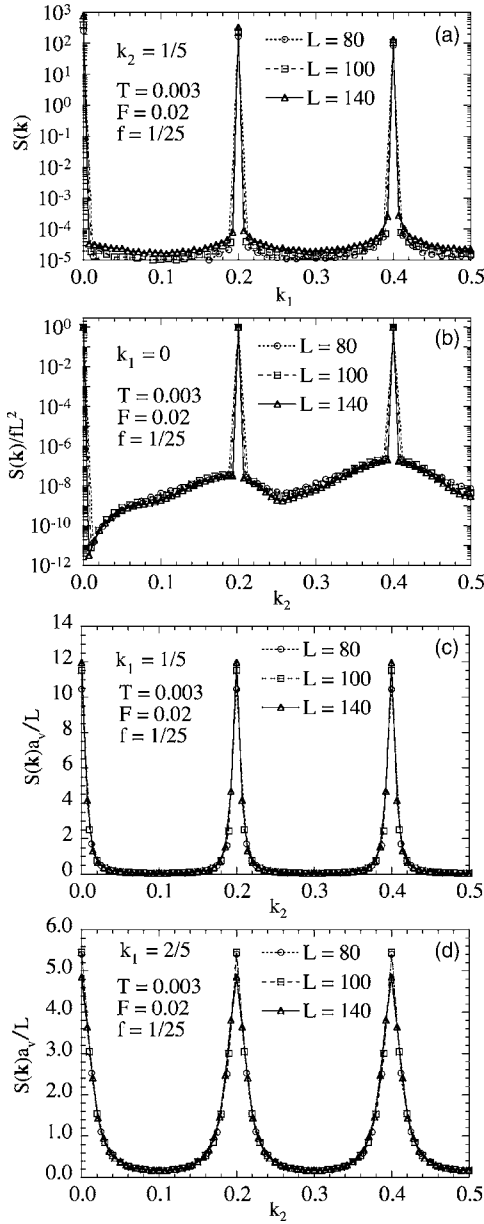


FIG. 12. Profiles of  $S(\mathbf{k})$  in various directions, for different system sizes  $L$ , for the smectic phase at  $F=0.02$ ,  $T=0.003$ . (a)  $S(\mathbf{k})$  vs  $k_1$  for fixed  $k_2=1/5$ ; (b)  $S(\mathbf{k})/fL^2$  vs  $k_2$  for fixed  $k_1=0$ ; (c)  $S(\mathbf{k})a_0/L$  vs  $k_2$  for fixed  $k_1=1/5$ ; (d)  $S(\mathbf{k})a_0/L$  vs  $k_2$  for fixed  $k_1=2/5$ . Note the logarithmic scale in (a) and (b).

crease in  $\xi_{\perp}$  as  $T \rightarrow 0$ . In the liquid,  $\xi_{\perp}$  and  $\xi_{\parallel}$  are comparable.

### C. Smectic phase—Low drive

We now consider the structure of the smectic in the limit of smaller driving forces, in particular the case  $F=0.02$ ,  $T=0.003$ , shown in Fig. 4(c). In Fig. 12 we plot profiles of  $S(\mathbf{k})$  along different paths in the first Brillouin zone, for different system sizes  $L \times L$ . Comparing with the analogous Fig. 7 for the high drive case,  $F=0.1$ , we see that the peaks are now more sharply defined. The peaks along the  $k_2$  axis at  $k_1=0$  in Fig. 12(b) continue to look like Bragg peaks, being

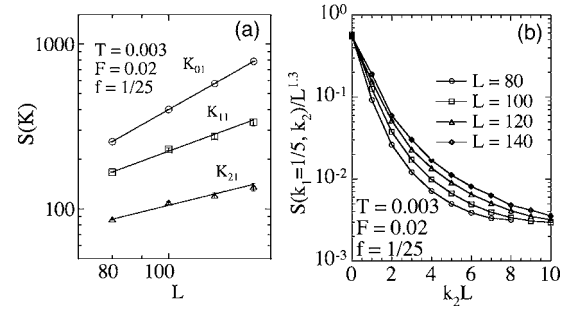


FIG. 13. Smectic phase at low drive,  $F=0.02$ ,  $T=0.003$ . (a) Scaling of peak heights  $S(\mathbf{K})$  vs system size  $L$ . Straight lines indicate good power-law fits  $S(\mathbf{K}) \sim L^s$ , with  $s \approx 2.0$  for  $\mathbf{K}_{01}$ ,  $s \approx 1.3$  for  $\mathbf{K}_{11}$ , and  $s \approx 0.87$  for  $\mathbf{K}_{21}$ . (b) Attempted scaling collapse of  $S(k_1=1/5, k_2)/L^{1.3}$  vs  $k_2L$ .

only one grid point wide and with heights scaling as  $L^2$ , thus indicating long-range ordering into smectic channels. However the peak heights at finite  $k_1=1/5, 2/5$  in Figs. 12(c) and 12(d) no longer appear to scale  $\sim L$  as do the corresponding peaks in Fig. 7.

In Fig. 13(a) we plot the heights of various peaks  $S(\mathbf{K})$  versus  $L$  for various system sizes  $L \times L$ . While the smectic peak  $S(\mathbf{K}_{01})$  scales  $\sim L^2$  as expected, we find  $S(\mathbf{K}_{11}) \sim L^{1.3}$ , more divergent than the  $\sim L$  behavior found at higher drive. This suggests the possibility of longer range, perhaps algebraic, correlations between the different smectic channels. For algebraically diverging peaks, however, we expect that not only the peak height must scale, but the entire peak profile should scale. The expected scaling relation is<sup>17</sup>

$$S(k_1=1/5, k_2) \sim L^{1.3} f(k_2L), \quad (37)$$

where  $f(x)$  is a scaling function. In Fig. 13(b) we test this scaling prediction by plotting  $S(k_1=1/5, k_2)/L^{1.3}$  versus  $k_2L$  for different sizes  $L$ . We clearly do *not* find the scaling collapse expected for algebraic correlations.

To explain the above behavior, we consider the transverse correlation function  $C(k_1=1/5, m_2)$ , which we plot versus  $m_2$  for different system sizes  $L \times L$  in Fig. 14(a). The solid lines are fits to the periodic exponential of Eq. (35), and give the values  $\xi_{\perp} \approx 29.6, 30.8, 29.7$  for sizes  $L=80, 100, 140$ , respectively. Our results thus consistently indicate short-range order between the smectic channels, with a finite transverse correlation length  $\xi_{\perp} \approx 30$ . The absence of the expected  $\sim L$  scaling in Figs. 12(c) and 12(d) is then a finite size effect due to the correlation length  $\xi_{\perp}$  being comparable to the system length  $L$ .

We similarly estimate the longitudinal correlation length by plotting  $C(m_1, m_2=0)$  versus  $m_1$ , for different system sizes  $L \times L$ , in Fig. 14(b). Fitting to the periodic exponential of Eq. (36), with  $c_1=1/5$  and  $c_2=4/5$ , we find  $\xi_{\parallel} \sim 4700$ . We conclude that the smectic phase at small drive is qualitatively the same as that at large drive, except for having larger, but still finite, correlation lengths.

Finally we consider behavior as the driving force  $F$  varies. In Fig. 15(a) we plot the transverse correlation function  $C(k_1=1/5, m_2)$  versus  $m_2$ , for  $T=0.003$  in a  $60 \times 60$  system, for various values of  $F$  from the low drive case considered

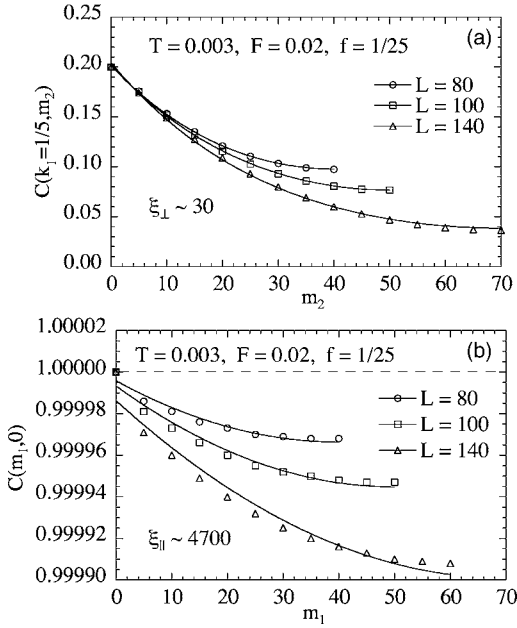


FIG. 14. Smectic phase at low drive  $F=0.02$ ,  $T=0.003$ , for various system sizes  $L \times L$ . (a) Transverse correlation function  $C(k_1=1/5, m_2)$  vs  $m_2$  and (b) longitudinal correlation function  $C(m_1, m_2=0)$  vs  $m_1$ . Solid lines are fits to periodic exponentials as in Eqs. (35) and (36) and determine the correlation lengths  $\xi_{\perp}$  and  $\xi_{\parallel}$ .

above,  $F=0.02$ , to the high drive case considered previously,  $F=0.1$ . Solid lines are fits to the periodic exponential of Eq. (35). In Fig. 15(b) we plot the corresponding longitudinal correlation function  $C(m_1, m_2=0)$  versus  $m_1$ . Solid lines are fits to the periodic exponential of Eq. (36), with  $c_1=1/5$  and  $c_2=4/5$ . From these fits we estimate the transverse and longitudinal correlation lengths,  $\xi_{\perp}$  and  $\xi_{\parallel}$ , which are plotted in Figs. 16(a) and 16(b). We see that the transverse correlation length  $\xi_{\perp}$  grows as  $F$  decreases below 0.05. For  $F \geq 0.05$ ,  $\xi_{\perp}$  levels off to a constant,  $\xi_{\perp} \sim 7$ . In fact, for  $F \geq 0.05$ , the transverse correlation  $C(k_1=1/5, m_2)$  shown in Fig. 15(a) is completely independent of  $F$ . The longitudinal correlation length  $\xi_{\parallel}$  grows exponentially as  $F$  decreases below 0.04, has a shallow minimum at  $F=0.05$  [presumably related to the minimum in the melting line  $T_m(F)$  that occurs nearby] and then saturates to a constant above  $F=0.06$ . The longitudinal correlation  $C(m_1, m_2=0)$  shown in Fig. 15(b) is independent of  $F$  for  $F > 0.06$ . These results strongly suggest that no new behavior will be seen by increasing  $F$  to even larger values, and we have verified this explicitly by simulating up to  $F=2.0$ .

The above cross over point between low and high drives, and its value  $F_{cr} \approx 0.05$ , can be understood from Fig. 2(b). Consider the system in its  $F=0$  ground state. The interaction energy to move a given charge forward parallel to  $\mathbf{F}$  is  $\Delta\mathcal{H}_1 \approx 0.0627$ ; the rate to make this move is  $W = W_0 e^{-(\Delta\mathcal{H}_1 - F)/2T}$ . Once this charge has moved forward, the interaction energy to move the neighboring charge in the same row forward is  $\Delta\mathcal{H}_2 \approx 0.0270$ ; the rate to make this move is  $W_f = W_0 e^{-(\Delta\mathcal{H}_2 - F)/2T}$ . This needs to be compared against the rate for the first charge to move back to its origi-

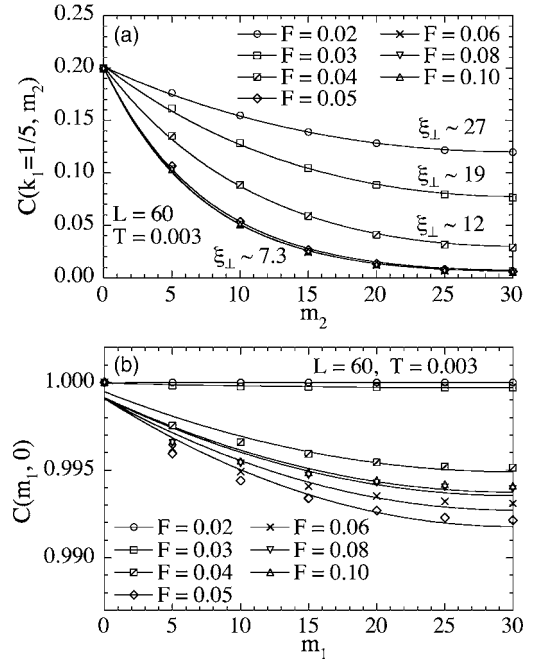


FIG. 15. Smectic phase at  $T=0.003$ , for various driving forces  $F$  in a  $60 \times 60$  size system. (a) Transverse correlation function  $C(k_1=1/5, m_2)$  vs  $m_2$  and (b) longitudinal correlation function  $C(m_1, m_2=0)$  vs  $m_1$ . Solid lines are fits to periodic exponentials as in Eqs. (35) and (36) and determine the correlation lengths  $\xi_{\perp}$  and  $\xi_{\parallel}$ .

nal position  $W_b = W_0 e^{(\Delta\mathcal{H}_1 - F)/2T}$ . The ratio of these last two rates is

$$\frac{W_f}{W_b} = e^{(2F - \Delta\mathcal{H}_1 - \Delta\mathcal{H}_2)/2T}, \quad (38)$$

and so the two rates are equal when  $F_{cr} = (\Delta\mathcal{H}_1 - \Delta\mathcal{H}_2)/2 = 0.045$ , which agrees with our observations in Figs. 15 and 16. When  $F > F_{cr}$ , the probability that the neighboring charge moves forward along with the first charge is larger than the probability that the first charge falls back into place. Once the second charge moves forward, the remaining charges in the row will follow suite. Therefore when  $F \gg F_{cr}$ , virtually *all* moves are those which advance a charge in the direction of the applied force  $\mathbf{F}$ ; charges in the smectic channels move continuously forward row by row. For  $F < F_{cr}$ , charges which

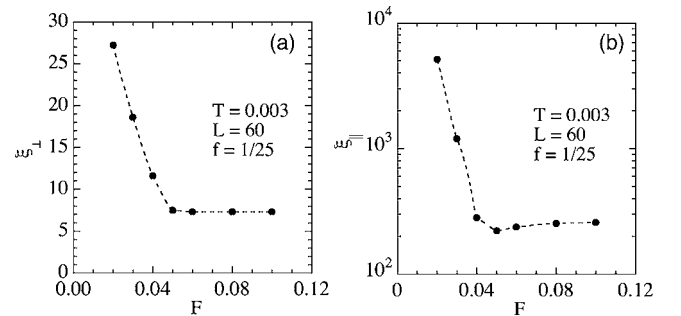


FIG. 16. (a) Transverse correlation length  $\xi_{\perp}$  and (b) longitudinal correlation length  $\xi_{\parallel}$  vs  $F$ , at  $T=0.003$  for a  $60 \times 60$  system.

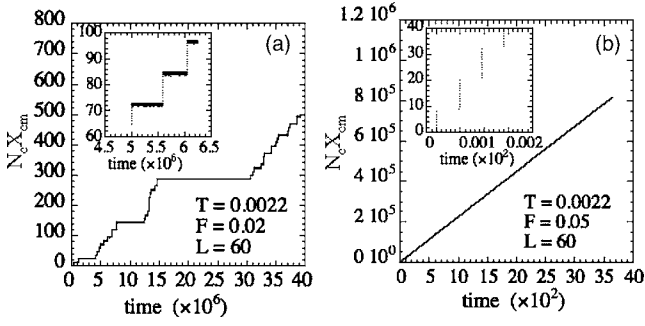


FIG. 17. Center of mass displacement parallel to the driving force for  $T=0.0022$ ,  $L=60$ .  $N_c X_{c.m.}$  vs simulation clock time  $t$  for (a)  $F=0.02$  and (b)  $F=0.05$ . The insets show an expanded picture on a short time scale.

advance forward parallel to  $\mathbf{F}$  will more often than not fall backwards to their original position on the next move. The system spends finite time with no net motion, in between randomly occurring avalanches that advance an entire row of charges forward. The result is a stick-slip type of motion.

The above scenario is illustrated in Fig. 17 where we plot the center of mass displacement parallel to  $\mathbf{F}$  times the number of charges  $N_c X_{c.m.}$  versus the simulation clock time  $t$ . We show results for  $T=0.0022$ , slightly lower than the temperature 0.003 considered above, for a system of size  $60 \times 60$ . Figure 17(a), for  $F=0.02 < F_{cr}$ , shows the steplike advancement forward of the system, characteristic of stick-slip motion. The inset shows an expanded scale for short time. The height of each step is exactly 12 grid spacings, corresponding to the advance of all 12 charges in a given smectic channel. Along the plateau of each step we see motion one grid space forward, followed by one grid space backwards, with no net motion. In Fig. 17(b) we show results for  $F=0.05 \geq F_{cr}$ . We see that motion is perfectly linear in time. The inset shows that the system moves smoothly forward, with one row advancing immediately after another.

#### D. Liquid phase

We now briefly consider the liquid phase. The liquid phase shown in Fig. 4(b), at  $F=0.02$ ,  $T=0.008$ , appears fairly structureless. However as  $T$  decreases, and the finite correlation lengths grow, local structure develops. As discussed in Sec. III B the melting line  $T_m(F)$  decreases as the size of the system increases. Although, for  $L=60$ ,  $T_m(F)$  always lies above  $T=0.003$  [see Fig. 3(b)], when  $L$  increases, the minimum of  $T_m(F)$  near  $F \sim 0.03$  dips below 0.003. In Fig. 18 we plot the structure function  $S(\mathbf{k})$  for a system of size  $120 \times 120$  at  $T=0.003$  and driving force  $F=0.05$ . Although one sees prominent peaks at the reciprocal lattice vectors corresponding to the  $F=0$  ground state, the system is in a liquid state with short-range translational order. The heights of the peaks are small compared to those in a more ordered (i.e., smectic or solid) state, and as  $L$  increases, the peak heights stay finite rather than diverging with system size.

Next we consider how behavior in the liquid varies with the driving force  $F$ . In Fig. 19(a) we plot the longitudinal and transverse correlation lengths  $\xi_{\perp}$  and  $\xi_{\parallel}$  versus  $F$ . We obtain

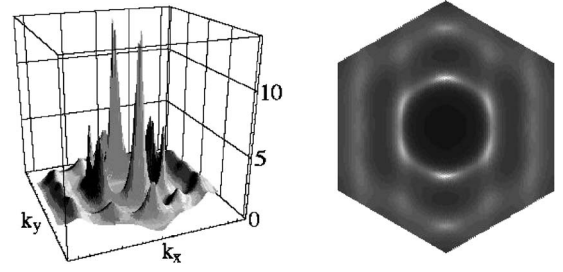


FIG. 18. Structure function  $S(\mathbf{k})$  for a system of size  $120 \times 120$  in the liquid state at  $T=0.003$  and  $F=0.05$ .

$\xi_{\parallel}$  and  $\xi_{\perp}$  by fitting to the correlation functions  $C(m_1, m_2 = 0)$  and  $C(x=0, y)$  in the same way as we have done earlier in constructing Fig. 11. We see that  $\xi_{\perp}$  and  $\xi_{\parallel}$  increase with increasing  $F$ , and that  $\xi_{\perp} \sim 2\xi_{\parallel}$ . That order extends further in the transverse than the longitudinal direction can be seen by noting that the transverse peaks in  $S(\mathbf{k})$ , shown in Fig. 18, are larger than the peaks with a longitudinal component. The same observation was made in our earlier work<sup>8</sup> for a much larger system at higher driving force.

We also investigate orientational order in the liquid. In Fig. 19(b) we plot the absolute value of the sixfold orientational order parameter  $|\langle \Phi_6 \rangle|$  versus  $F$  at  $T=0.003$ , for several different system sizes  $L \times L$ . Depending on the value of  $L$  and the corresponding value of  $T_m(F; L)$ , the system is either in the smectic state (with a high value of  $|\langle \Phi_6 \rangle|$ ) or in the liquid state (with a low value of  $|\langle \Phi_6 \rangle|$ ). Even in the liquid  $|\langle \Phi_6 \rangle|$  is finite because of the sixfold rotational symmetry of the underlying triangular grid. We see that, as  $F$  increases in the liquid,  $|\langle \Phi_6 \rangle|$ , similar to  $\xi_{\perp}$  and  $\xi_{\parallel}$ , increases. Thus both translational and orientational order in the liquid increase as the driving force  $F$  increases.

#### E. Dynamics

The preceding sections have dealt with the structural behavior of the driven system. In this section we consider some of the dynamical behavior. In Fig. 20 we plot results for the average velocity  $v_{ave, x}$  parallel to the driving force  $\mathbf{F}=F\hat{x}$ , for a  $60 \times 60$  size system. In Fig. 20(a) we show results for fixed  $F=0.10 > F_{cr}$ , in the high drive limit, versus  $1/T$ . The dashed

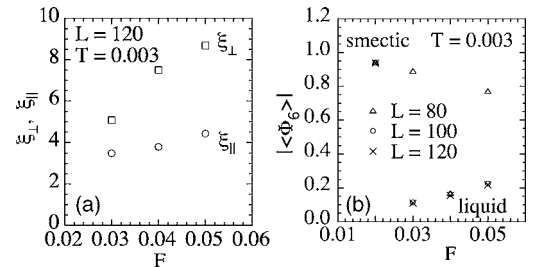


FIG. 19. (a) Correlation lengths  $\xi_{\perp}$  and  $\xi_{\parallel}$  vs  $F$  for a system of size  $120 \times 120$  in the liquid state at  $T=0.003$ . (b) Orientational order parameter  $|\langle \Phi_6 \rangle|$  vs  $F$  for several systems of size  $L \times L$  at  $T=0.003$ . The larger valued data points are for the smectic phase; the lower data points are for the liquid phase.

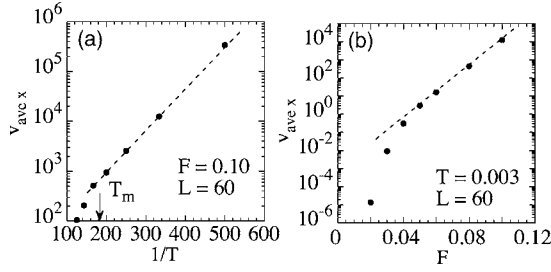


FIG. 20. Average velocity  $v_{ave,x}$  parallel to the driving force  $F$  for a  $60 \times 60$  system. (a)  $v_{ave,x}$  vs  $1/T$  for fixed  $F=0.10$  in the high drive limit. (b)  $v_{ave,x}$  vs  $F$  for fixed  $T=0.003$  in the smectic. The dashed lines indicate the exponential dependence of  $v_{ave,x}$  on  $F$  and  $1/T$ .

line for  $1/T_m < 1/T$  shows the exponential dependence on  $1/T$  in the smectic phase  $v_{ave,x} \sim e^{T_0/T}$ . Fitting to this form we find  $T_0 \approx 0.02$ . We can understand this value as follows. As discussed in Sec. III C, at such high  $F$  virtually all moves in CTMC result in the advance of a charge forward; the charges in the smectic channels move steadily forward one channel at a time. The average velocity is set by the rate for the charges in a given channel to move forward, which in turn is set by the rate for the first charge in the channel to move forward (all other charges in that channel moving forward on a much more rapid time scale). The rate for the first charge in a channel to move forward is  $\sim e^{-\Delta U_{min 1}/2T}$ , where  $-\Delta U_{min 1} = F - \Delta \mathcal{H}_1$ , with  $\Delta \mathcal{H}_1 \approx 0.06$  from Fig. 2(b). Thus we have  $T_0 = (F - \Delta \mathcal{H}_1)/2 = 0.02$ .

In Fig. 20(b) we show results for  $v_{ave,x}$  vs  $F$ , for fixed  $T = 0.003 < T_m$ , in the smectic phase. The dashed line shows the exponential dependence on  $F$  in the high drive limit,  $F > F_{cr} \approx 0.045$ ,  $v_{ave,x} \sim e^{F/F_0}$ . From the preceding discussion, we expect  $F_0 = 2T = 0.006$ , and we find this value gives an excellent fit to the data.

We have also considered the dependence of the average velocity on the system size. In Table I we list the values of  $v_{ave,x}$  for various system sizes, with different aspect ratios  $L_1/L_2$ , at  $F=0.10$ ,  $T=0.004$ , in the high drive smectic. In agreement the discussion at the end of Sec. II B 3 we see that  $v_{ave,x}$  scales roughly proportional to the length of the system  $L_1$  parallel to the driving force.

Next we consider the diffusion of the center of mass about its average motion. To compute  $\mathbf{D}(t)$  we need to compute the correlation between states of the system separated by time  $t$ . Since we are interested in the long  $t$  limit, computing  $\mathbf{D}(t)$  accurately thus requires much longer simulations than were needed to compute the structural (equal time) correlations. We therefore present results only for several typical cases. In Fig. 21 we plot  $D_{yy}(t)$  and  $D_{xx}(t)$ , defined by Eq. (33), versus the simulation clock time  $t$ , for the smectic in the low drive

TABLE I. Average velocity  $v_{ave,x}$  for various system sizes on a triangular grid at  $F=0.10$ ,  $T=0.004$ , in the high drive smectic.

$L_1$	60	60	120	120	120	240
$L_2$	30	60	30	60	120	60
$v_{ave,x}$	2569	2550	4971	4930	4978	7135

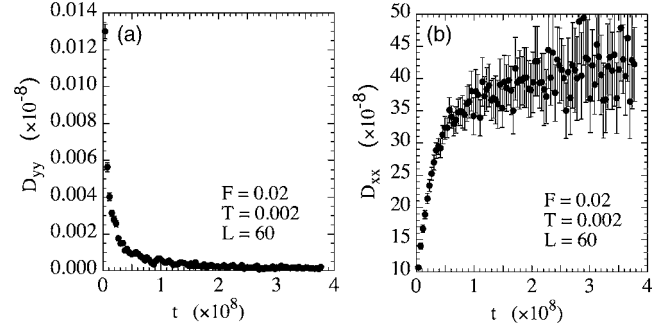


FIG. 21. Center-of-mass diffusion constants (a)  $D_{yy}$  and (b)  $D_{xx}$  vs time  $t$  for the smectic phase in the low drive limit  $F=0.02$ ,  $T=0.002$  for a system of size  $60 \times 60$ . That  $D_{yy} \rightarrow 0$  indicates the system is transversely pinned.

limit of  $F=0.02$ ,  $T=0.002$ , for a  $60 \times 60$  size system. We see that  $D_{yy}$  decays to zero, indicating that the system is transversely pinned.  $D_{xx}$  saturates to a finite constant as  $t$  increases, indicating a random walk motion about the average center of mass position. In Fig. 22 we similarly plot  $D_{yy}$  and  $D_{xx}$  for the smectic in the high drive limit of  $F=0.05$ ,  $T=0.0022$ . Again we see that  $D_{yy} \rightarrow 0$  and the system is transversely pinned, while  $D_{xx}$  saturates to a finite constant. In Fig. 23 we plot  $D_{yy}$  and  $D_{xx}$  for the liquid at  $F=0.10$ ,  $T=0.006$ , just above the melting transition. In this case both  $D_{yy}$  and  $D_{xx}$  approach finite constants as  $t$  increases; as expected, the liquid is not transversely pinned.

Since both  $D_{xx}$  and  $v_{ave,x}$  approach constants in the long time limit, a convenient measure of the strength of fluctuations about the average motion is given by  $D_{xx}/v_{ave,x}$ . For the low drive smectic of Fig. 21 we find  $D_{xx}/v_{ave,x} \approx 40$ . This is consistent with our interpretation of this region as being one of stick-slip motion. In this case we expect that the motion of rows of charges forward will constitute a Poisson process with avalanches occurring at a rate  $\lambda$ . At each avalanche  $n_r \sqrt{f}L$  charges move forward, where  $\sqrt{f}L$  is the number of charges in a given smectic channel, and  $n_r$  is the number of correlated channels. The average center of mass displacement in time  $t$  is then  $\Delta X_{c.m.} = (n_r \sqrt{f}L / N_c) \lambda t = (n_r / [\sqrt{f}L]) \lambda t$ , where we used  $N_c = fL^2$  is the total number of charges. Because it is a Poisson process, the variance of the number of avalanches is equal to the average, and so the fluctuation

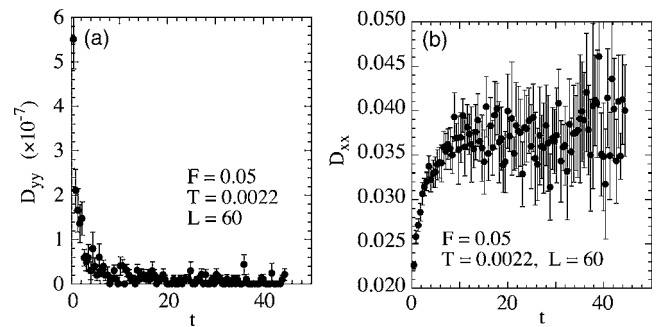


FIG. 22. Center of mass diffusion constants (a)  $D_{yy}$  and (b)  $D_{xx}$  vs time  $t$  for the smectic phase in the high drive limit  $F=0.05$ ,  $T=0.0022$ , for a system of size  $60 \times 60$ . That  $D_{yy} \rightarrow 0$  indicates the system is transversely pinned.



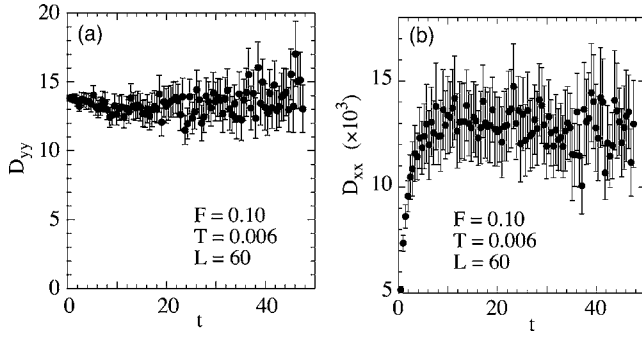


FIG. 23. Center of mass diffusion constants (a)  $D_{yy}$  and (b)  $D_{xx}$  vs time  $t$  for the liquid phase at  $F=0.10$ ,  $T=0.006$ , for a system of size  $60 \times 60$ .

about this average displacement is  $(\Delta X_{c.m.})^2 = (n_r / [\sqrt{fL}])^2 \lambda t$ . This yields the ratio  $D_{xx}/v_{ave x} = N_c (\Delta X_{c.m.})^2 / 2 \Delta X_{c.m.} = n_r \sqrt{fL}/2$ . For  $f=1/25$  and  $L=60$  we get  $D_{xx}/v_{ave x} = 6n_r$ . At low  $T$  and  $F$  the correlation length  $\xi_{\perp}$  can get large (see Fig. 16); if several channels are correlated, the ratio 40 can be attained.

For the high drive case of Fig. 22, we find the ratio  $D_{xx}/v_{ave x} \approx 0.00025$ . In this limit where rows of channels move steadily forward one after the other, longitudinal fluctuations are greatly suppressed. Finally, for the liquid case of Fig. 23, we find  $D_{xx}/v_{ave x} \approx 25$ . In the liquid, the system is structurally disordered and the motion of the charges is largely uncorrelated. Fluctuations about the center-of-mass motion are correspondingly enhanced.

#### IV. RESULTS ON A SQUARE GRID

We now consider the behavior of the driven Coulomb gas on a periodic square grid of sites. We consider only CTMC dynamics for the same charge density of  $f=1/25$  that was considered above for the triangular grid. We first consider behavior in the limit  $T \rightarrow 0$ . In Fig. 24(a) we show the equilibrium ground-state configuration for  $F=0$ . The charges occupy the sites of a  $5 \times 5$  square sublattice of the grid. The basis vectors of this sublattice,  $\mathbf{c}_1 = 3\hat{x} - 4\hat{y}$  and  $\mathbf{c}_2 = 4\hat{x} + 3\hat{y}$ , are clearly *not* aligned with the grid basis vectors  $\hat{a}_1 = \hat{x}$  and  $\hat{a}_2 = \hat{y}$ , nor with the driving force  $\mathbf{F} = F\hat{x}$  that we apply. This will produce some interesting effects.

When  $F > F_c \approx 0.06$  the charges will start to move forward parallel to  $\mathbf{F}$ , according to the order in which they most lower the system energy. In Fig. 24(a) we number the charges in the order in which they move in a particular CTMC pass, and in Fig. 24(b) we give the change in interaction energy  $\Delta\mathcal{H}$  associated with each move, as was done for the triangular grid in Fig. 2. Charges move forward in the  $\hat{x}$  direction in an order dictated by their position along the  $\mathbf{c} = \mathbf{c}_1 + \mathbf{c}_2$  direction, as indicated by the arrow drawn in Fig. 24(a). If one follows a path along the direction of  $\mathbf{c}$ , using periodic boundary conditions, one finds that the path closes upon itself only after one has passed through all the charges in the ground state. Thus there is no row by row motion as there was for the case of the triangular grid, and hence no oscillation in  $\Delta\mathcal{H}$  as a function of simulation step.

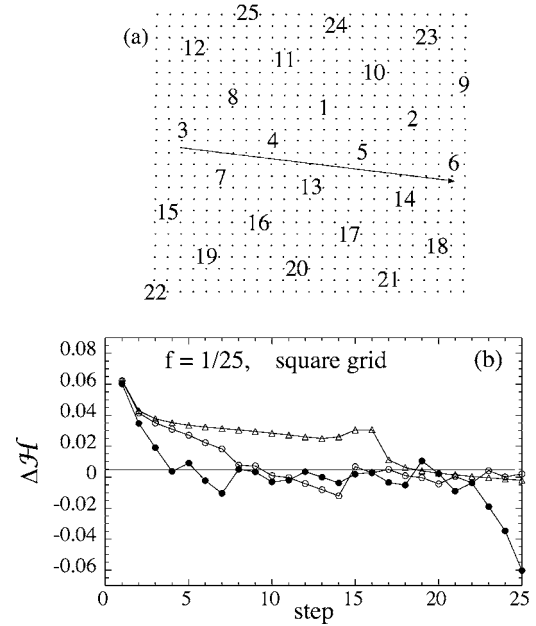


FIG. 24. CTMC on a square grid with charge density  $f=1/25$  at  $T \rightarrow 0$  and  $F > F_c$ , with  $\mathbf{F}$  parallel to the  $\hat{a}_1$  axis. (a) Ground-state charge lattice for a  $25 \times 25$  square grid. The numbers denote the locations of the charges in the ground state. The value of each number indicates the step on which that charge moves forward. (b) The change in interaction energy  $\Delta\mathcal{H}$  at each step as charges move forward.  $\bullet$  is for a  $25 \times 25$  grid and correspond to the moves in (a);  $\circ$  and  $\triangle$  are the beginnings of similar sequences for  $50 \times 50$  and  $100 \times 100$  grids.

#### A. High drive

We now consider behavior at finite temperature and high drive. We simulate a  $50 \times 50$  size system, starting from the  $F=0$  ground state, at the values  $T=0.004$ ,  $F=0.10$ . In Fig. 25(a) we show an intensity plot of the structure function  $S(\mathbf{k})$  at the initial stage of the simulation; our results are averaged over  $1250$  CTMC passes after an initial  $2500$  passes were discarded for equilibration. We see peaks at wave vectors  $\mathbf{K}$  corresponding to the ordered  $F=0$  ground state. The peaks remain sharp in the  $k_1$  direction, but are somewhat smeared out in the transverse  $k_2$  direction, suggesting a moving lattice with anisotropic translational correlations. If we simulate longer, however, this moving ground-state lattice undergoes a change of structure. In Fig. 25(b) we show  $S(\mathbf{k})$  averaged over  $5 \times 10^6$  passes, after discarding an initial  $5 \times 10^6$  passes. We see clearly a sixfold orientational order in the position of the peaks, which are aligned with one of the diagonals of the square grid. Figure 25(b) is reminiscent of the floating triangular lattice (algebraic translational order) that is seen in *equilibrium* simulation<sup>6</sup> of more dilute systems on a square grid, however without a finite size scaling analysis we cannot be certain of the nature of translational order in the system. Finally, however, if we simulate even longer, the structure changes yet again to a smectic phase with channels oriented parallel to  $\mathbf{F}$ . In Fig. 25(c) we show  $S(\mathbf{k})$  averaged over  $2.5 \times 10^7$  passes, after discarding an initial  $3.75 \times 10^7$  passes. We see clearly the same smectic structure that we saw for the triangular grid in Fig. 4(d). The extremely long (compared to

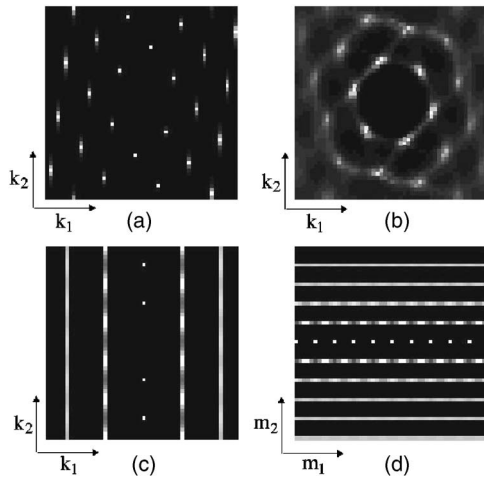


FIG. 25. (a)–(c) Intensity plot of structure function  $S(\mathbf{k})$  for a  $50 \times 50$  size system at  $T=0.004$ ,  $F=0.1\hat{a}_1$ , starting from the ground state of Fig. 24(a). (a)  $S(\mathbf{k})$  averaged over 3750 passes, after an initial 2500 passes of equilibration; (b)  $S(\mathbf{k})$  averaged over  $5 \times 10^6$  passes, after discarding an initial  $5 \times 10^6$  passes; (c)  $S(\mathbf{k})$  averaged over  $2.5 \times 10^7$  passes, after discarding an initial  $3.75 \times 10^7$  passes. (d) Intensity plot of real space correlations  $C(m_1, m_2)$  corresponding to the smectic  $S(\mathbf{k})$  of (c).

the triangular grid) time it takes for the system to order into the smectic results because the initial ground-state configuration is ordered with a set of reciprocal lattice vectors  $\{\mathbf{K}\}$  that is not commensurate with that of the final state smectic. The system first requires a long time to disorder the initial state, and then another long time to reorder into the smectic.

We have checked the above results by carrying out simulations in which we start from an initial random configuration of charges. After roughly  $3.5 \times 10^7$  passes, we find that the system orders into the same smectic state as in Fig. 25(c). In Fig. 25(d), we show an intensity plot of the real space correlations in the smectic  $C(m_1, m_2)$  obtained from the Fourier transform of the  $S(\mathbf{k})$  of Fig. 25(c). We see that charges in the same channel ( $m_2=0$ ) have a sharp periodic ordering. Correlations between channels show that the charges in neighboring channels are staggered; the peak in charge density in one channel aligns with the minimum in charge density of the neighboring channel, so as to form a local ordering that is more triangular than square. As one moves to channels further away, the correlations decrease and the peaks in  $C(m_1, m_2)$  get smeared out.

We now check that the smectic phase of Fig. 25(c) has the same scaling behavior with system size that was found for the triangular grid. For larger systems with  $L=100$ – $200$ , it is not possible to simulate for the very long times ( $\sim 10^7$  passes) that are needed to order into the smectic from either the ground state or a random initial state. We therefore start with an initial configuration that is a periodic repetition of the smectic state for  $L=50$ , and simulate for only relatively short times. For  $L=100, 150$ , and  $200$ , we use 10 000, 2000, and 2000 passes. Our results are shown in Fig. 26, where we plot the profiles of  $S(\mathbf{k})$  along different paths through the first Brillouin zone. Figure 26(a) shows that the peaks are as sharply confined to the values  $k_1=1/5, 2/5$  as was found for

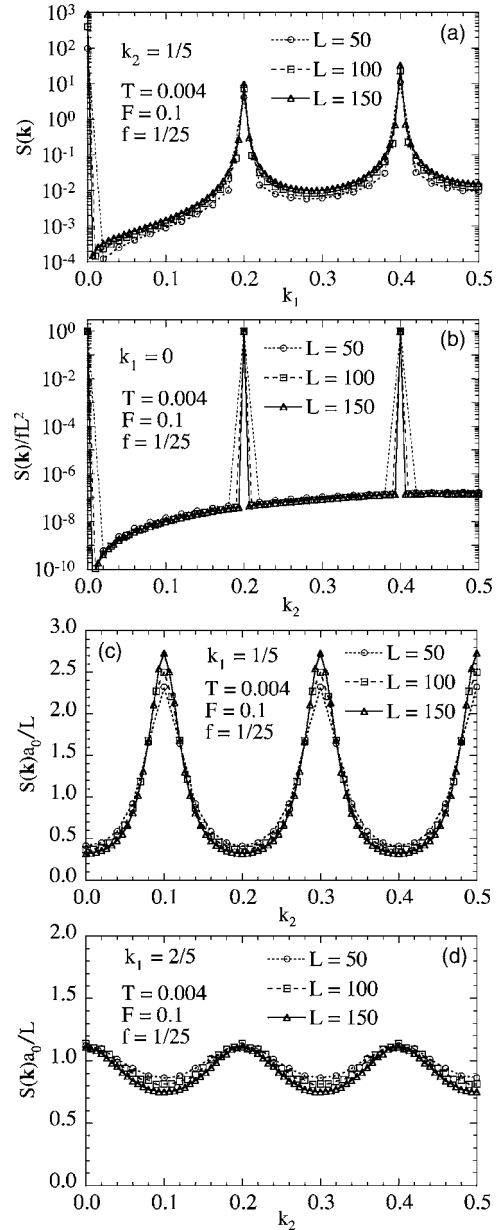


FIG. 26. Profiles of  $S(\mathbf{k})$  in various directions, for different system sizes  $L$ , for the smectic phase at  $F=0.10$ ,  $T=0.004$  on a square grid. (a)  $S(\mathbf{k})$  vs  $k_1$  for fixed  $k_2=1/5$ ; (b)  $S(\mathbf{k})/fL^2$  vs  $k_2$  for fixed  $k_1=0$ ; (c)  $S(\mathbf{k})a_0/L$  vs  $k_2$  for fixed  $k_1=1/5$ ; (d)  $S(\mathbf{k})a_0/L$  vs  $k_2$  for fixed  $k_1=2/5$ . Note the logarithmic scale in (a) and (b).

the triangular grid. Figure 26(b) shows that the peaks at  $k_1=0$  scale  $\sim L^2$ , indicating long-range smectic order. Figures 26(c) and 26(d), show that  $S(k_1, k_2)$  for fixed  $k_1=1/5, 2/5$  scales roughly  $\sim L$ . Note that the scaling collapse in Fig. 26(c) is not quite as nice as the corresponding Fig. 7(c) for the triangular grid. Plotting the peak value  $S(\mathbf{K}_{11})$  versus  $L$ , similar to what was done in Fig. 6, gives  $S(\mathbf{K}_{11}) \sim L^s$  with  $s \approx 1.17$ . We believe that this value  $s > 1$ , rather than being a signature of stronger correlations between smectic channels, may just reflect the persistence of correlations introduced by our initial periodic configuration, which have not yet completely washed out over our relatively short runs.

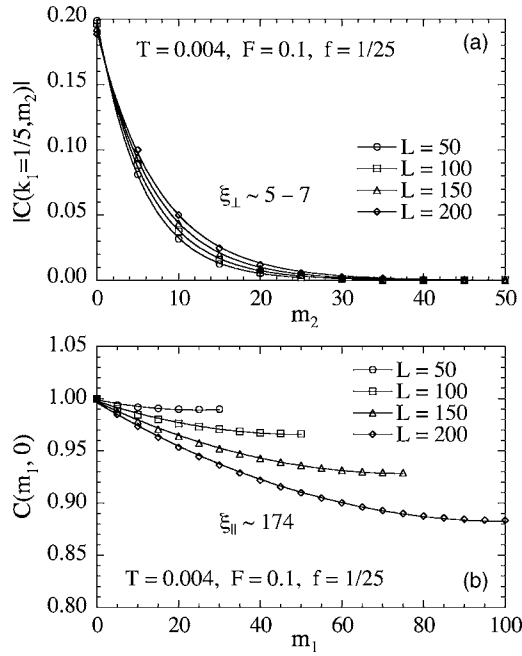


FIG. 27. Transverse and longitudinal correlation functions at  $F=0.1$ ,  $T=0.004$ , for system sizes  $L \times L$  on a square grid. (a)  $|C(k_1=1/5, m_2)|$  at values  $m_2=5n$ ,  $n$  integer, for different sizes  $L$ ; solid lines are fits to the periodic exponential of Eq. (35). (b)  $C(m_1, m_2=0)$  at values  $m_1=5n$ ,  $n$  integer, for different sizes  $L$ ; solid lines are fits to the periodic exponential of Eq. (36).

In Fig. 27 we plot the transverse and longitudinal correlation functions, obtained from the appropriate Fourier transform of  $S(\mathbf{k})$ .  $C(k_1=1/5, m_2)$  in Fig. 27(a) shows exponentially decaying transverse correlations, with a correlation length  $\xi_{\perp} \sim 5-7$ , comparable to that found for the triangular grid at the same parameter values. We believe that the slight increase from  $\xi_{\perp} \approx 5$  to 7 as  $L$  increases from 50 to 200 reflects the correlations introduced by our initial configuration, as already commented on in connection with Fig. 26(c). Note that the peak values of  $C(k_1=1/5, m_2)$  oscillate in sign for successive values of  $m_2=5n$ ,  $n$  integer, due to the  $\pi$  phase shift from channel to channel that is apparent in the real space correlations shown in Fig. 25(d); hence we have plotted  $|C(k_1=1/5, m_2)|$  in Fig. 26(a). In Fig. 27(b) we plot the longitudinal correlation  $C(m_1, m_2=0)$ . The solid lines are fits to a periodic exponential, and give a common value of  $\xi_{\parallel} \approx 174$  for all sizes  $L$ . Thus we have a finite correlation length, but  $\xi_{\parallel} \sim L$ . We conclude that the driven steady state for low  $T$  and large  $F$  on the square grid is a smectic that is qualitatively the same as what was found for the triangular grid.

### B. Low drive

We now consider behavior at low drive, simulating at  $T=0.004$ ,  $F=0.04$  for an  $L \times L$  system of size  $L=75$ . We will find that these parameters place the system right at the melting transition. We start from an initial random configuration and run  $2.5 \times 10^4$  passes to equilibrate, followed by  $2.5 \times 10^7$  passes to compute averages. In Fig. 28 we plot the

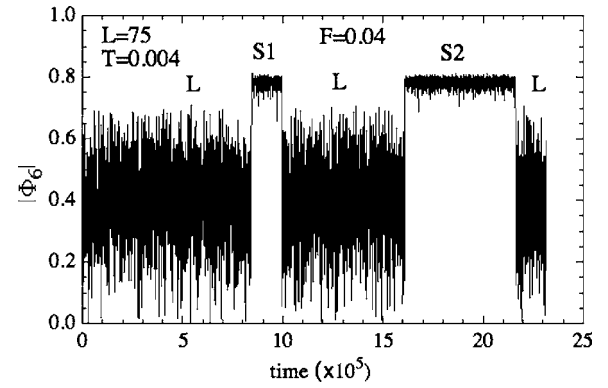


FIG. 28. Sixfold orientational order parameter  $|\Phi_6|$  vs simulation clock time  $t$  for  $T=0.004$ ,  $F=0.04$  and  $L \times L$  system of size  $L=75$ . Regions denoted “L” are in a moving liquid state; regions denoted “S1” and “S2” are in a moving solid state. Coexistence of the two states indicates that the system is at the melting transition.

instantaneous absolute value of the sixfold orientational order parameter  $|\Phi_6|$  versus the simulation clock time  $t$ . We see that the system makes sharp jumps between states of lower and higher values of  $|\Phi_6|$  and conclude that these are the coexisting liquid and ordered phases at the first order melting transition. In Fig. 29(a) we show an intensity plot of the structure function  $S(\mathbf{k})$  averaged over only the liquid states labeled “L” in Fig. 28. We see a liquidlike  $S(\mathbf{k})$ , but with a striking sixfold modulation of intensity in the diffuse peaks, corresponding to the relatively large values of  $|\Phi_6| \sim 0.4$  seen in Fig. 28. In Fig. 29(b) we show  $S(\mathbf{k})$  averaged over the ordered states labeled “S2” in Fig. 28. We see periodic sharp

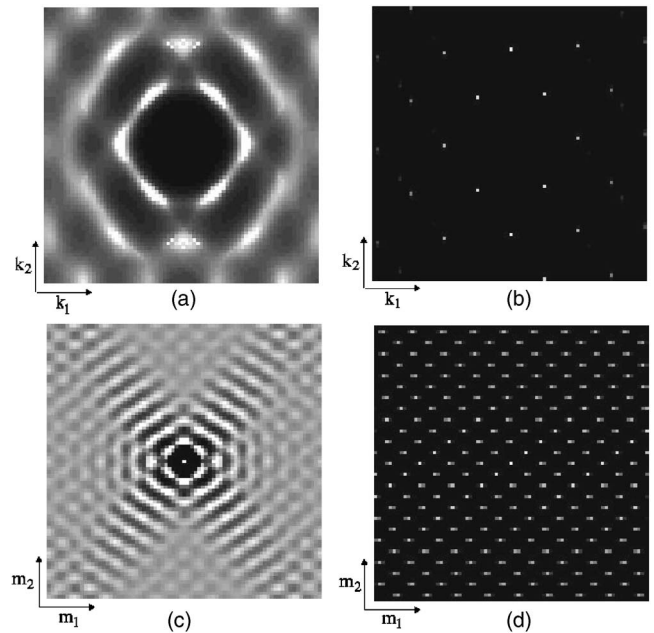


FIG. 29. Intensity plots of  $S(\mathbf{k})$  at  $T=0.004$ ,  $F=0.04$ , for an  $L \times L$  system of size  $L=75$  averaged over (a) the liquid states labeled “L” and (b) the solid states labeled “S2” of Fig. 28. Intensity plots of the corresponding real space correlations  $C(\mathbf{r})$  for (c) the liquid states “L” and (d) the solid states “S2.” The applied force  $\mathbf{F}$  is in the horizontal direction.

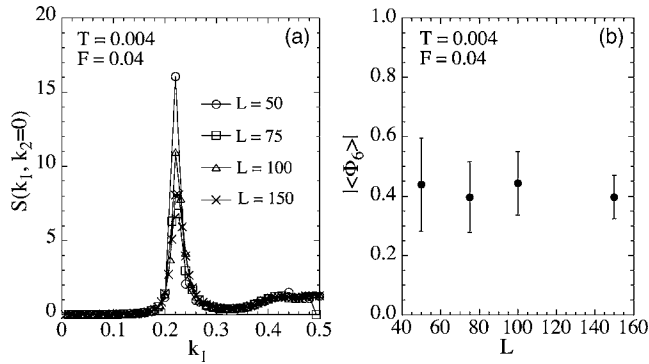


FIG. 30. The liquid state at  $T=0.004$ ,  $F=0.04$  for different  $L \times L$  system sizes. (a)  $S(k_1, k_2=0)$  vs  $k_1$ ; (b) six-fold orientational order parameter  $|\langle \Phi_6 \rangle|$  vs  $L$ ; bars denote the standard deviation of the distribution of  $|\Phi_6|$ .

peaks suggesting a moving solid state.  $S(\mathbf{k})$  for the states labeled “S1” in Fig. 28 is identical to that of Fig. 29(b), except reflected about the  $k_2$  axis. In Figs. 29(c) and 29(d) we show intensity plots of the corresponding real space correlations  $C(\mathbf{r})$ .

We consider first the liquid state. In Fig. 30(a) we plot  $S(k_1, k_2=0)$  versus  $k_1$  for several different  $L \times L$  system sizes. Except for the maximum of the first peak, we see essentially no finite size effect. The height of the first peak is different for the different  $L$ , however, there is no systematic variation with  $L$ ; we believe that these differences are just statistical fluctuations. We conclude that this state is a liquid with only short range translational order. Figures 28 and 29(a), however, suggest that the liquid may possess finite orientational order. In Fig. 30(b) we therefore plot  $|\langle \Phi_6 \rangle|$  versus  $L$  for the liquid state. We see that  $|\langle \Phi_6 \rangle|$  is roughly independent of  $L$ , confirming that the liquid has long-range hexatic orientational order.

The long-ranged hexatic liquid that we find in Fig. 29(a) is reminiscent of the long-ranged hexatic liquid found for the triangular grid at low temperatures, as shown in Fig. 18. There are, however, some important differences. A liquid in a continuum will always have *local* six-fold orientational order. However, due to the short-ranged translational correlations, the phase of the local complex orientational order parameter will vary with position. For a normal liquid, this causes correlations of the six-fold orientational order parameter to decay exponentially with distance. According to the theory of melting in two dimensions by Halperin and Nelson, and by Young,<sup>18</sup> there may also be an algebraically ordered hexatic liquid between the solid and normal liquid phases, in which correlations of the six-fold orientational order parameter decay algebraically. When the system sits on an external periodic potential, however, the local six-fold orientational order parameter can lock onto the symmetry directions of the external potential, which therefore serves as an ordering field for orientational order. For a triangular grid, the local six-fold order of the particles locks onto the six-fold rotational symmetry of the grid, as illustrated in Fig. 31(a). The result is long-range six-fold orientational order, with a finite  $\langle \Phi_6 \rangle$ . For a square grid, the local six-fold order of the particles may lock onto *either* the vertical *or* the horizontal directions of

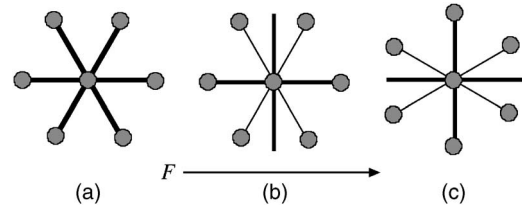


FIG. 31. Schematic showing how particle clusters with local six-fold orientational order (shaded circles connected by thin lines) may align with the rotational symmetry of an external potential or grid (thick lines). (a) lock in of the cluster to a six-fold rotationally invariant triangular grid; (b) lock in of the cluster to the horizontal axis of a four-fold rotationally invariant square grid; and (c) lock in to the vertical axis of a square grid.

the grid, as illustrated in Figs. 31(b) and 31(c). For a liquid in equilibrium, both of these orientations will occur in equal numbers on average. Since the two orientations are related by a  $\pi/2$  rotation, the relative phase of the six-fold orientational order parameter for the two cases is  $\exp(i6\pi/2) = -1$ , and adding them in equal numbers causes  $\langle \Phi_6 \rangle$  to vanish. A square grid induces no six-fold orientational order in equilibrium. For a liquid in a driven nonequilibrium steady state, however, the direction of the driving force  $\mathbf{F}$  breaks the symmetry between the vertical and horizontal directions, and can cause one to be favored over the other. A driving force therefore can lead to a finite  $\langle \Phi_6 \rangle$  and long-range six-fold orientational order on the square grid. From the plot of the real space correlation  $C(\mathbf{r})$  shown in Fig. 29(c), we see that the system locks onto the *vertical* direction, as in Fig. 31(c). The resulting structure function  $S(\mathbf{k})$ , shown in Fig. 29(a) has a set of six peaks about the origin, which are oriented so that one pair of the peaks align with the direction parallel to the applied driving force  $\mathbf{F}$ . This is in contrast to case for the triangular grid, shown in Fig. 18, where the peaks are oriented so that one pair of the peaks align with the direction transverse to the applied force.

We now consider the ordered moving state, labeled “S2” in Fig. 28. The structure function  $S(\mathbf{k})$ , and the real space correlations  $C(\mathbf{r})$  are shown in Figs. 29(b) and 29(d), respectively. Note that the periodic peaks in  $S(\mathbf{k})$  for this ordered state do *not* have the same symmetry as that of the equilibrium ground state. The latter [see Fig. 25(a)] consists of a *square* array of Bragg peaks, while in Fig. 29(b) the peaks are distorted into a more triangular structure. From either the location of the peaks in  $S(\mathbf{k})$ , or more easily from a direct inspection of the real space correlation  $C(\mathbf{r})$ , we see that this state consists of periodic channels of charges oriented parallel to the applied force  $\mathbf{F}$  in the  $\hat{a}_1 = \hat{x}$  direction. Within each channel the charges are ordered with an average separation of  $8/3$  grid spacing, while the channels themselves are separated from each other by three grid spacings. The nearest neighbors to a given charge are located in its two nearest neighboring channels, rather than within the same channel, reflecting a similar orientation of hexatic order as in the liquid. This can be compared with the smectic state at high drive, shown in Fig. 25(d). This smectic has channels in which charges are separated by five spaces, while the channels themselves are separated by five spaces; the nearest



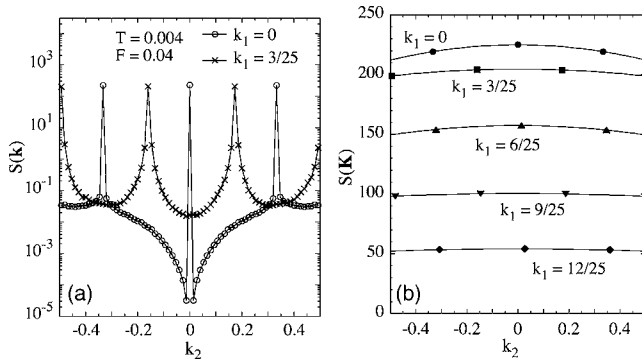


FIG. 32. Moving ordered phase of Fig. 29(b), for  $T=0.004$ ,  $F=0.04$ , and  $L=75$ . (a) Profiles of  $S(k_1, k_2)$  vs  $k_2$  showing the peaks at  $k_1=0$  and  $k_1=3/25$ ; note the logarithmic scale. (b) Heights of the dominant peaks in  $S(k_1, k_2)$  vs  $k_2$ ; the different curves represent different values of  $k_1$  and the solid lines are fits to a Gaussian.

neighbors to a given charge are located within the same channel. In contrast, the equilibrium ground state of Fig. 24(a) can be thought of as channels in which charges are separated by 25 spaces, while the channels themselves are separated by 1 space; nearest-neighbor charges lie in the next-next-nearest neighboring channels. The structure in terms of channels, as described above, is determined by the strength of the correlations between the channels. When channels are more strongly correlated, it can be energetically favorable to have the channels spaced more closely together, with a correspondingly larger distance between charges within a given channel; the stronger correlations between the channels will keep charges within neighboring channels from approaching each other too closely. The equilibrium ground state represents the extreme limit of long-range correlations between channels. The high drive smectic represents the opposite limit where correlations between channels are very short ranged and it becomes favorable to keep the spacing between channels at the same distance as the spacing of charges within a channel. The moving state of Fig. 29(d) can thus be thought of as having a structure, and presumably channel correlations, intermediate between these two limits.

The strong correlations between channels, as discussed above, are clearly evident in the plots of  $S(\mathbf{k})$  and  $C(\mathbf{r})$  in Figs. 29(b) and 29(d). All peaks in  $S(\mathbf{k})$  appear sharp in both the longitudinal and transverse directions; real space correlations  $C(\mathbf{r})$  appear to extend the entire length of the system in both longitudinal and transverse directions. This suggests a moving solid rather than a smectic. To investigate this further we consider in more detail the peaks in the structure function  $S(\mathbf{k})$ . In Fig. 32(a) we plot profiles of  $S(k_1, k_2)$  versus  $k_2$ , showing the peaks at  $k_1=0$  and  $k_1=3/25$ . For  $k_1=0$  the peaks appear as sharp  $\delta$ -function peaks upon a smooth background, similar to what was seen in Fig. 26(b) for the smectic at large drive, indicating the periodicity of the channels in the direction transverse to the driving force  $\mathbf{F}$ . At finite  $k_1=3/25$  the peaks are much sharper than the corresponding finite  $k_1$  peaks for the smectic at large drive in Fig. 26(c); in the present case the peaks drop by three orders of magnitude from maximum to minimum (note the logarithmic scale) and have a half width of about  $\Delta k \approx 0.007$ . Such sharp peaks

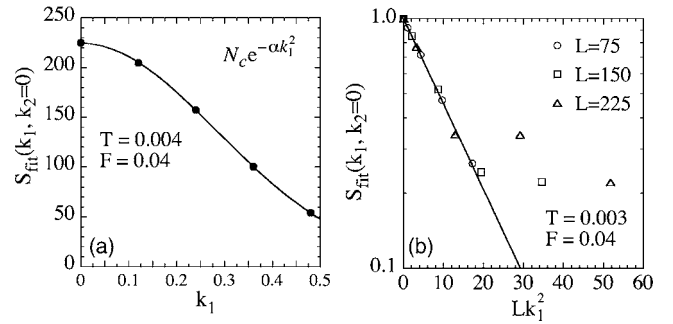


FIG. 33. (a) Moving ordered phase of Fig. 29(b), for  $T=0.004$ ,  $F=0.04$ , and  $L=75$ . Values  $S_{\text{fit}}(k_1, k_2=0)$  of fits from Fig. 32(b) vs  $k_1$ . Solid line is a fit of the data to a Gaussian. (b) Moving ordered phase for  $T=0.003$ ,  $F=0.04$ , and sizes  $L=75$ , 150, and 225. Values of  $S_{\text{fit}}(k_1, k_2=0)$  vs  $Lk_1^2$ . Solid line is a fit of the small  $k_1$  data to a straight line.

suggest the possible presence of long ranged or algebraic correlations between the channels.

In Fig. 32(b) we plot only the heights of the dominant peaks in  $S(k_1, k_2)$  versus  $k_2$ , for the different values of  $k_1$ . We see that at fixed  $k_1$ , there is only a very small variation of the peak heights with  $k_2$ ; however, the dependence on  $k_1$  is considerable. Fitting the points for each value of  $k_1$  to a simple Gaussian [the solid lines in Fig. 32(b)] we plot the resulting  $S_{\text{fit}}(k_1, k_2=0)$  versus  $k_1$  in Fig. 33(a), where another simple Gaussian  $S_{\text{fit}}(k_1, 0) = N_c \exp(-\alpha k_1^2)$  gives an excellent fit [the solid line in Fig. 33(a)]. Such a Gaussian shape for the peak heights is consistent with a Debye-Waller-like behavior for thermal fluctuations of a solid.

However, to investigate more precisely the nature of translational correlations, we need to investigate the dependence of the peak heights on system size  $L$ . We have *not*, however, been able to do this at  $T=0.004$ ; when, for larger system sizes  $L$ , we start the system off in an initial disordered state, we were unable to see a similar transition to an ordered state as was found in Fig. 28 for  $L=75$ . We assume that this is either because the melting temperature becomes somewhat lower for larger  $L$  (as was seen for the triangular grid), or perhaps because the free energy barrier between the liquid and ordered states increases with  $L$  and we have not run sufficiently long to have a thermal excitation over this barrier.

We choose, therefore, to investigate the finite size behavior at the lower temperature  $T=0.003$ , taking as an initial state an appropriate cut out of, or periodic extension of, the ordered state we found for  $T=0.004$ . For sizes  $L=50$  and  $L=100$ , when we started the system in such an initial state, we found that the system quickly melted to a liquid. We believe that this is because these values of  $L$  are not commensurate with the spacing of three grid spaces between channels required by this ordered structure. Ordered systems of size  $L=75$ , 150, and 225, however, remained stable. Proceeding similarly to Fig. 32(b), we examine the peak heights of  $S(k_1, k_2)$  versus  $k_2$  for the various  $k_1$ . At this lower temperature  $T=0.003$ , the variation with  $k_2$  is even smaller than that seen in Fig. 32(b) at  $T=0.004$ . Fitting to a Gaussian, we determine the values of  $S_{\text{fit}}(k_1, k_2=0)$  and fit these to a

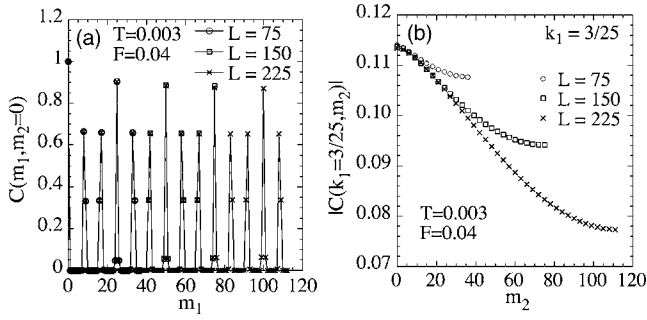


FIG. 34. Real space correlation for the moving ordered phase at  $T=0.003$ ,  $F=0.04$ , and  $L=75, 150, 225$ . (a) Longitudinal correlation  $C(m_1, m_2=0)$  vs  $m_1$ . (b) Transverse correlation  $|C(k_1=3/25, m_2)|$  vs  $m_2$ , for  $m_2=3n$ ,  $n$  integer.

Gaussian,  $S_{\text{fit}}(k_1, 0) = N_c \exp[-\alpha(L)k_1^2]$ , where  $N_c = fL^2$ . We find the surprising result that  $\alpha(L) \sim L$ . To show this, we plot in Fig. 33(b)  $S_{\text{fit}}(k_1, 0)/N_c$ , on a log scale, versus  $Lk_1^2$ . We see that the data at small  $k_1$  give an excellent collapse to a straight line. This exponential decrease in  $S(\mathbf{K})/N_c$  with increasing  $L$  suggests that the observed moving solid may not persist as a stable state in the large  $L$  limit.

We can also examine the translational order from the perspective of the real space correlations. In Fig. 34(a) we plot the longitudinal correlations  $C(m_1, m_2=0)$  versus  $m_1$ , for system sizes  $L=75, 150$ , and  $225$ . We clearly see that there are three charges for every 25 grid spacings. No finite size effect is seen. In Fig. 34(b) we plot the absolute value of the complex correlation  $C(k_1=3/25, m_2)$  versus  $m_2$ , showing values for only every third grid spacing,  $m_2=3n$ ,  $n$  integer. Here we find a pronounced finite size effect, with the correlation decaying to lower values as  $L$  increases. However a periodic exponential [as used for example in Fig. 27(a)] does not give a particularly good fit, and we do not have enough sizes  $L$  to try any systematic scaling fit. While the results of Figs. 33(b) and 34(b) thus suggest that long-range solid order may not persist as  $L$  increases, larger sizes will be needed to clarify the true large  $L$  behavior.

The structure that we have found in Figs. 29(b) and 29(d) for the ordered moving state at low drive has neither the commensurability with respect to the underlying grid of the equilibrium ground state, nor the large drive smectic. One can speculate that at other values of  $F$  and  $T$ , in this low-temperature ordered region, yet other commensurabilities may be found. Exploring the complete phase diagram of the driven lattice Coulomb gas on the square grid may therefore prove to be considerably more challenging than was for the case of the triangular grid, and we leave this for future investigations.

### C. Dynamics

We now consider some of the dynamic properties for the driven Coulomb gas on the square grid. We will not attempt a detailed calculation of diffusion constants, as we did for the triangular grid, however, we will still be able to make some interesting observations by looking at average velocity and center-of-mass motion. We first consider the case of the high

TABLE II. Average velocity  $v_{\text{ave},x}$  in the high drive smectic state for various system sizes  $L \times L$  at  $F=0.10$ ,  $T=0.004$ , on the square grid.

$L$	100	150	200
$v_{\text{ave},x}$	1082	1617	2065

drive smectic  $F=0.10$ ,  $T=0.004$ , considered in Sec. IV A. In Table II we give the values for the average center of mass velocity parallel to the driving force  $v_{\text{ave},x}$  for various system sizes  $L \times L$ . Similar to our results for the triangular grid (see Table I) we find  $v_{\text{ave},x} \sim L$  scales proportional to the length of the system in the direction of the applied force, in agreement with the discussion at the end of Sec. II B 3. Inspection of the center-of-mass motion as a function of time clearly shows no transverse diffusion, indicating that the smectic is transversely pinned, just as we found for the triangular grid.

Next we consider the case of low drive,  $F=0.04$ , considered in Sec. IV B. We consider first the case at melting,  $T=0.004$  and  $L=75$ , where the system is making transitions between the liquid and a more ordered state, as shown in Fig. 28. In Fig. 35(a) we plot the component of the instantaneous center of mass displacement parallel to the driving force  $X_{\text{c.m.}}$  versus the simulation clock time  $t$ . Light lines denote times in which the system is in the liquid state, while heavy lines denote times when the system is in the ordered state (compare with Fig. 28). That the lines in each region of time are perfectly straight indicates a constant average velocity  $v_{\text{ave},x}$  in each region. Note, however, that the velocity in the ordered state is slightly larger than that in the liquid state: in the liquid,  $v_{\text{ave},x}=10.05$ , while in the ordered state,  $v_{\text{ave},x}=11.50$ , or 14% larger. In Fig. 35(b) we plot the transverse component of the center-of-mass displacement  $Y_{\text{c.m.}}$  versus the simulation clock time  $t$ . In the liquid,  $Y_c$  shows the noisy fluctuations characteristic of diffusion; the observed bias towards increasing values of  $Y_{\text{c.m.}}$  we believe is just a statistical fluctuation. In the ordered phase, however,  $Y_{\text{c.m.}}$  stays essentially constant indicating that the system is transversely pinned.

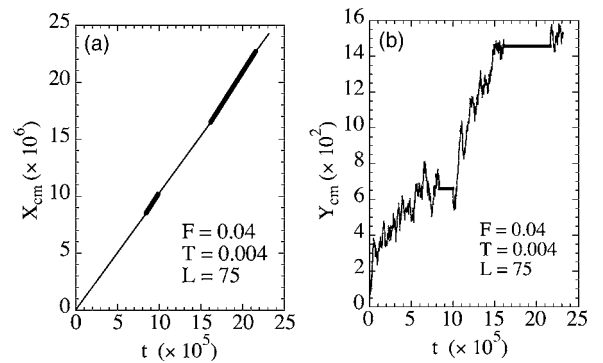


FIG. 35. Center of mass displacement for  $F=0.04$ ,  $T=0.004$ , and system size  $L=75$ , at the melting transition: (a) motion parallel to  $\mathbf{F}$ ,  $X_{\text{c.m.}}$  vs time  $t$ ; (b) motion transverse to  $\mathbf{F}$ ,  $Y_{\text{c.m.}}$  vs  $t$ . Light lines correspond to times when the system is in the liquid state. Heavy lines correspond to times when the system is the ordered state (see Fig. 28).

TABLE III. Average velocity  $v_{ave,x}$  in the ordered phase at various system sizes  $L \times L$  for  $F=0.04$ ,  $T=0.003$ , on the square grid.

$L$	75	150	225
$v_{ave,x}$	36.3	36.3	36.1

We now consider the ordered phase at the lower temperature  $T=0.003$ . In Table III we give the values of  $v_{ave,x}$  for systems of different sizes  $L \times L$ . We consider only the values  $L=75$ , 150, and 225 that result in an ordered moving state. In contrast to the high drive smectic (see Table II) we now find that  $v_{ave,x}$  is independent of  $L$ . This at first seems paradoxical, since the ordered state at low drive is more strongly correlated than the smectic at high drive. However it may be that the incommensurability of the ordered state in the parallel direction (where the average spacing between charges is  $8\frac{1}{3}$  grid spacings) is sufficient to remove the energy barriers responsible for the avalanche effects (see Sec. II B 3) that give rise to the  $v_{ave,x} \sim L_1$  dependence in the high drive smectic. Finally, an examination of the transverse displacement, similar to that of Fig. 35(b), shows that the ordered state is transversely pinned.

## V. DISCUSSION AND CONCLUSIONS

In this work we have applied lattice gas dynamics to model the nonequilibrium steady states of a driven diffusive system, the 2D classical lattice Coulomb gas in a uniform applied force. We have considered two different dynamic algorithms, and have found that they result in qualitatively different phase diagrams, contrary to naive expectations. We have shown that the commonly used driven diffusive Metropolis Monte Carlo (DDMMC) algorithm results in a structurally disordered moving steady state over most of the phase diagram. We have argued that this is due to unphysical intrinsic randomness in the algorithm that remains even as  $T \rightarrow 0$ .

We have then applied the continuous time Monte Carlo (CTMC) algorithm to the driven diffusive problem and found it to produce smectic and, for the square grid, possibly more strongly correlated steady states at low temperatures. We have shown (Appendix ) that CTMC is a natural discretization of continuum Langevin dynamics. We have argued (Sec. II B 2) that in general it gives a physically correct dynamics when the grid sites are regarded as the minima of an external one-body potential  $U(\mathbf{r})$ , and the energy barriers  $U_0$  of this potential remain larger than the energy change  $\Delta E$  in hopping between neighboring minima, so that motion is by thermal activation of one particle at a time over the potential barriers. It remains unclear whether or not CTMC will be qualitatively correct in the very large drive limit  $\Delta E > U_0$  when the applied force overcomes the pinning force of the potential, and the minima of the corresponding washboard potential  $U(\mathbf{r}) - \mathbf{F} \cdot \mathbf{r}$  vanish. In such a case, for a *spatially uniform* system in an initially ordered state, each charge will experience an equal net force forward from the washboard potential, and one would expect at low temperatures that the charges would move coherently together. The CTMC algo-

rithm, which only moves a single charge at a time, breaks this spatial uniformity and might introduce unphysical effects. For the case of a system with *quenched randomness*, however, the random pinning already breaks spatial uniformity, and the forces on the charges will in general be different. In such a case, the single particle moves of the CTMC algorithm may not be as unphysical. This very large drive limit for the case of random pinning has been the subject of numerous recent theoretical<sup>15,19,20,21</sup> and numerical<sup>17,21-27</sup> works.

For CTMC we have shown (Sec. III B) that diverging correlation lengths as  $T \rightarrow 0$  can give rise to subtle finite size effects that can be difficult to detect with the usual finite size scaling methods applied to the peaks of the structure function  $S(\mathbf{K})$  and we have argued that the smectic state that we find for finite size systems will become unstable to a liquid on sufficiently large length scales. However, since the relevant correlation lengths diverge as  $T \rightarrow 0$ , the smectic will be the stable steady state in any finite system, at sufficiently low temperature. We have also shown that, on a square grid, long-range hexatic orientational order develops in the moving steady state liquid, and that this is a purely nonequilibrium effect.

The one component 2D lattice Coulomb gas serves as a model for logarithmically interacting point vortices in a 2D superconducting network, or a superconducting film with a periodic potential. Driven vortices in a 2D periodic potential at *finite* temperature have been simulated by several others using *continuum* dynamics. The molecular dynamic simulations of Reichhardt and Zimányi<sup>28</sup> and of Carneiro<sup>29</sup> used square periodic pins embedded in a flat continuum, with a number of vortices equal to, or greater than, the number of pins. We do not expect that such models, in which a sizable fraction of the vortices spend most of their time in the flat space between the pins, will be well described by our dilute density of charges on a discrete grid, where all charges spend most of their time at the potential minima.

Much closer to our model is that of Marconi and Domínguez<sup>30,31</sup> who simulate the dynamics of a square array of Josephson junctions using resistively shunted-junction (RSJ) dynamics applied to a 2D XY model. They study a vortex density per unit cell of the array of  $f=1/25$ , the same density as used in our present work. The phase diagram which they report has some qualitative similarity to our own phase diagram of Fig. 3(b), with an ordered, transversely pinned, moving state at low temperatures.<sup>32</sup> However, in contrast to either the smectic we find at high drives [see Fig. 25(c)] or the more ordered state we find at low drives [see Fig. 29(b)], they find a moving vortex lattice where  $S(\mathbf{k})$  has peaks at the *same* reciprocal lattice vectors  $\mathbf{K}$  as the equilibrium ground state. From a finite size scaling analysis of  $S(\mathbf{K})$  using  $L=50$ , 100, and 150, they conclude that their state is a vortex lattice with anisotropic algebraically decaying translational correlations.

To understand possible reasons for the difference between their results and ours, we first consider the relevant parameters of their model. For their cosine Josephson junction model, the effective one-body potential<sup>33</sup> that the array structure introduces for vortex motion has an energy barrier  $U_0 \approx 0.12$ , in units where the Josephson coupling energy is  $J_0$



=1. Many of Marconi and Domínguez's results are in the limit where the force  $F$  (i.e., the applied current in the Josephson array model) satisfies  $F > U_0$ . This is the case where the minima in the washboard potential parallel to the driving force have vanished, and where we have argued that our lattice gas dynamics might not apply. However, even for the case  $F < U_0$ , the two models may be in different parameter regimes. Our lattice gas dynamics implicitly assumes that the energy barrier  $U_0$  is larger than all other energy scales. For the Josephson array of Marconi and Domínguez, however, a direct calculation using the XY model shows that the energy to move a single vortex forward one grid space from its ground-state position is  $\Delta E_1 \approx 0.34$ , substantially bigger than the barrier  $U_0 \approx 0.12$ . Our simulations are therefore in the limit of a much stronger pinning potential.

In spite of these parameter differences, we can still make some observations. First we note that Marconi and Domínguez always begin their simulations from the equilibrium ground state (or states evolved from it); they are unable to cool the system from a liquid and find the ordered state, hence there is no independent check that the state they find is the true stable steady state. Next, we note that because their simulations use a continuum dynamics, they are unable to simulate for the very long times that are possible using our lattice gas dynamics. As a measure of the effective simulation time, we can compute the total displacement  $\Delta R_{c.m.}$  of the vortex center of mass parallel to the applied force over the total time of the simulation. For the Josephson array, if  $V$  is the average measured voltage drop per junction parallel to the applied current,  $I_0$  the critical current of a single junction,  $R_N$  the normal shunt resistance,  $f$  the vortex density, and  $\tau_J \equiv \hbar/(2eR_N I_0)$  the time constant, then  $\Delta R_{c.m.} = (V/I_0 R_N) \times (\Delta t/\tau_J)(N_t/2\pi f)$ , where  $\Delta t$  is the time integration step of the simulation, and  $N_t$  is the number of such steps. Using Marconi and Domínguez's values<sup>31</sup> of  $\Delta t/\tau_J = 0.1$ ,  $f = 1/25$ ,  $N_t = 10^5$ , and typical values<sup>31</sup> of  $V/I_0 R_N$  from their Fig. 5, we find for their simulations that  $\Delta R_{c.m.} \sim 1.2 \times 10^3$  grid spacings or less. In contrast, our simulations which lead to Fig. 25(c) have a total simulation time corresponding to  $\Delta R_{c.m.} \approx 6 \times 10^7$  grid spacings, more than four orders of magnitude larger. To make a better comparison with Marconi and Domínguez, we note that our results of Fig. 25(a), starting from the equilibrium ground state, correspond to a total center of mass displacement of only  $\Delta R_{c.m.} \approx 4 \times 10^3$  grid spacings, similar to that of Marconi and Domínguez. The state we find in Fig. 25(a) has peaks in  $S(\mathbf{k})$  at the same  $\mathbf{K}$  as the equilibrium ground state, moreover the anisotropies of this state are the same as for the state found by Marconi and Domínguez; the peaks develop a finite width in the direction transverse to the direction of motion [this feature is visible in Fig. 25(a)], and the heights of the peaks decrease as  $\mathbf{k}$  varies in the direction of motion. In our case the variation in peak heights is only a 20% reduction from largest to smallest, whereas for Marconi and Domínguez it is a larger 75%, nevertheless the behavior is qualitatively similar. It thus may be that the simulations of Marconi and Domínguez have not run long enough to observe the true long time steady state of the system.

Finally, we comment on one additional issue that is related to our ability, using lattice gas dynamics, to simulate to

much longer times that can be achieved with continuum methods. It is interesting to note in Fig. 23 that the longitudinal diffusion constant  $D_{xx}$  in the liquid approaches its long time limit on a much longer time scale than does the transverse diffusion constant  $D_{yy}$ . In recent continuum Langevin simulations<sup>34</sup> of driven vortices in a disordered 2D superconductor, similar diffusion in the vortex liquid phase was computed. Although it was observed that the transverse diffusion constant saturated to a finite value at long times, the longitudinal diffusion constant was found not to saturate, but rather to grow proportional to  $t$ . Rather than reflecting superdiffusive behavior in the longitudinal direction,<sup>34</sup> this result might simply be a failure to simulate to long enough times to see the longitudinal diffusion constant saturate.

## ACKNOWLEDGMENTS

We wish to thank D. Domínguez, M. C. Marchetti, and A. A. Middleton for helpful discussions. This work was supported by DOE Grant No. DE-FG02-89ER14017 and NSF grant PHY-9987413.

## APPENDIX

In this appendix we demonstrate that the transition rates of Eq. (13) correctly describe diffusive Langevin motion in the limit that the energy change in one move satisfies  $\Delta U \ll T$ . Our derivation follows one given earlier<sup>35</sup> for a single degree of freedom, and extends it to the case of many degrees of freedom.

The Langevin equation of motion for diffusively moving particles in a uniform driving force  $\mathbf{F}$  can be written as

$$\frac{\partial r_{i\alpha}}{\partial t} = -D \frac{\partial U}{\partial r_{i\alpha}} + \eta_{i\alpha}, \quad (\text{A1})$$

where  $r_{i\alpha}$  is the  $\alpha$  component of the position of particle  $i$ ,

$$U[\{\mathbf{r}_i\}] \equiv \mathcal{H}[\{\mathbf{r}_i\}] - \mathbf{F} \cdot \sum_i \mathbf{r}_i, \quad (\text{A2})$$

with  $\mathcal{H}$  the Hamiltonian giving the internal interactions between the particles, and  $\eta_{i\alpha}$  is the  $\alpha$  component of the thermally fluctuating force acting on particle  $i$ . In order that the system reaches equilibrium in the absence of the force  $\mathbf{F}$ , the thermal force is taken to have correlations

$$\langle \eta_{i\alpha}(t) \rangle = 0, \quad (\text{A3})$$

$$\langle \eta_{i\alpha}(t) \eta_{j\beta}(t') \rangle = 2DT \delta_{ij} \delta_{\alpha\beta} \delta(t - t'). \quad (\text{A4})$$

The corresponding Fokker-Planck equation that describes the probability  $P(\{\mathbf{r}_i\})$  for the system to be at coordinates  $\{\mathbf{r}_i\}$  is then given by

$$\frac{\partial P}{\partial t} = D \sum_{i\alpha} \left[ \frac{\partial}{\partial r_{i\alpha}} \left( P \frac{\partial U}{\partial r_{i\alpha}} \right) + T \frac{\partial^2 P}{\partial r_{i\alpha}^2} \right]. \quad (\text{A5})$$

Next we symmetrize the Fokker-Planck equation by making the transformation



$$\psi(\{\mathbf{r}_i\}) \equiv e^{U[\{\mathbf{r}_i\}]/2T} P(\{\mathbf{r}_i\}). \quad (\text{A6})$$

Substituting the above into the Fokker-Planck equation (A5) gives the imaginary time Schrödinger equation

$$\frac{\partial \psi}{\partial t} = DT \sum_{i\alpha} \left[ \frac{\partial^2 \psi}{\partial r_{i\alpha}^2} - V_{i\alpha} \psi \right], \quad (\text{A7})$$

where

$$V_{i\alpha} = \left[ \left( \frac{1}{2T} \frac{\partial U}{\partial r_{i\alpha}} \right)^2 - \frac{1}{2T} \frac{\partial^2 U}{\partial r_{i\alpha}^2} \right]. \quad (\text{A8})$$

If we now discretize the coordinates, so that the  $\mathbf{r}_i$  are confined to the sites of a periodic lattice, the natural way to discretize Eq. (A7) is to replace the second derivative of  $\psi$  with its lattice equivalent

$$\frac{\partial \psi}{\partial t} = DT \sum_i [\Delta_i^2 - V_i] \psi, \quad (\text{A9})$$

where  $\Delta_i^2$  is the discrete Laplacian for the lattice with respect to coordinate  $\mathbf{r}_i$  and  $V_i$  the appropriate discretization of  $\sum_\alpha V_{i\alpha}$ , as will be explained below. For a lattice with nearest neighbors given by the vectors  $\{\pm \hat{a}_\mu\}$ , the discrete Laplacian acting on a scalar function  $f(\mathbf{r})$  is defined by

$$\Delta^2 f(\mathbf{r}) \equiv c \sum_\mu [f(\mathbf{r} + \hat{a}_\mu) - 2f(\mathbf{r}) + f(\mathbf{r} - \hat{a}_\mu)], \quad (\text{A10})$$

with  $c$  an appropriate geometrical constant to give the correct continuum limit.

If we denote the state of the system with particles at positions  $\{\mathbf{r}_i\}$  as  $s$ , then we can write the above Eq. (A9) in a matrix form

$$\frac{\partial \psi_s}{\partial t} = \sum_{s'} \tilde{M}_{ss'} \psi_{s'}, \quad (\text{A11})$$

where the matrix  $\tilde{\mathbf{M}}$  has elements

$$\tilde{M}_{ss} = -DT[z c + V_i], \quad (\text{A12})$$

$$\tilde{M}_{ss'} = cDT \quad \text{when } s' = \{\mathbf{r}_i \pm \hat{a}_\mu, \mathbf{r}_j\}, \quad (\text{A13})$$

$$\tilde{M}_{ss'} = 0 \quad \text{otherwise}, \quad (\text{A14})$$

where  $z$  is the number of nearest-neighbor sites. By the notation in Eqs. (A13) and (A14) we mean that the only non-zero off-diagonal elements of  $\tilde{\mathbf{M}}$  are those connecting states  $s$  and  $s'$  in which only a single particle at  $\mathbf{r}_i$  has moved to a nearest neighbor position  $\mathbf{r}_i \pm \hat{a}_\mu$ , and all other particles have remained unchanged. This is our first result: the natural discretization of continuum Langevin dynamics to a lattice gas dynamics involves single particle moves only.

To see what are the correct single particle hopping rates for our lattice gas dynamics, as well as to see what is the correct discretized form for the  $V_i$  of Eq. (A9), consider now

the master equation for our lattice gas dynamics. If  $s = \{\mathbf{r}_i\}$  is the state of the system, then the probability  $P_s$  to be in state  $s$  is determined by

$$\frac{\partial P_s}{\partial t} = \sum_{s'} [W_{ss'} P_{s'} - W_{s's} P_s] \equiv \sum_{s'} M_{ss'} P_{s'}, \quad (\text{A15})$$

where  $W_{s's}$  is the rate to make a transition from state  $s$  to state  $s'$ . We therefore have

$$M_{ss} = - \sum_{s'} W_{s's}, \quad (\text{A16})$$

$$M_{ss'} = W_{ss'}, \quad s \neq s'. \quad (\text{A17})$$

We next apply the same transformation as in Eq. (A5), to get

$$\frac{\partial \psi_s}{\partial t} = \sum_{ss'} e^{U_s/2T} M_{ss'} e^{-U_{s'}/2T} \psi_{s'}. \quad (\text{A18})$$

Comparing with Eq. (A11) we get

$$\tilde{M}_{ss'} = e^{(U_s - U_{s'})/2T} M_{ss'}, \quad (\text{A19})$$

and from Eqs. (A13) and (A17) we then get for the off-diagonal elements of  $\tilde{\mathbf{M}}$ ,

$$\tilde{M}_{ss'} = e^{(U_s - U_{s'})/2T} W_{ss'} = cDT, \quad (\text{A20})$$

when the state  $s'$  differs from the state  $s$  by only a single particle that has moved to a nearest neighbor site, i.e.,  $\mathbf{r}_i \rightarrow \mathbf{r}_i \pm \hat{a}_\mu$ , with all other  $\mathbf{r}_j$  kept constant; all other off-diagonal terms vanish. The above result then determines the transition rates that are needed for the discrete master equation to model the continuum Langevin equation

$$W_{ss'} = cDT e^{-(U_s - U_{s'})/2T}. \quad (\text{A21})$$

Thus we arrive at the rates of Eq. (13) that define our CTMC algorithm.

Note that the rates of Eq. (A21) satisfy a local detailed balance

$$\frac{W_{ss'}}{W_{s's}} = e^{-(U_s - U_{s'})/T}. \quad (\text{A22})$$

Having determined the rates  $W_{ss'}$ , we can now determine the diagonal part of  $\tilde{\mathbf{M}}$  and hence the  $V_i$  of Eq. (A9). Defining  $\Delta U_{i\pm\mu}$  as the change in  $U$  when a single particle moves  $\mathbf{r}_i \rightarrow \mathbf{r}_i \pm \hat{a}_\mu$ , i.e.,

$$\Delta U_{i\pm\mu} \equiv U[\{\mathbf{r}_i \pm \hat{a}_\mu, \mathbf{r}_j\}] - U[\{\mathbf{r}_i, \mathbf{r}_j\}], \quad (\text{A23})$$

then Eqs. (A16) and (A19) give for the diagonal elements of  $\tilde{M}_{ss}$ ,

$$\tilde{M}_{ss} = M_{ss} = - \sum_{s'} W_{s's} \quad (\text{A24})$$

$$= -cDT \sum_{s'} e^{-(U_{s'} - U_s)/2T} \quad (\text{A25})$$

$$= -cDT \sum_{i\mu} [e^{-\Delta U_{i+\mu}/2T} + e^{-\Delta U_{i-\mu}/2T}]. \quad (\text{A26})$$

If one now expands Eq. (A26) to order  $(\Delta U/2T)^2$ , and then uses Eq. (A10) that  $c \sum_{\mu} (\Delta U_{i+\mu} + \Delta U_{i-\mu}) = \Delta_i^2 U$ , and compares to Eq. (A12), one concludes that

$$V_i = -\frac{\Delta_i^2 U}{2T} + \sum_{\mu} \left[ \frac{c}{2} \left( \frac{\Delta U_{i+\mu}}{2T} \right)^2 + \frac{c}{2} \left( \frac{\Delta U_{i-\mu}}{2T} \right)^2 \right]. \quad (\text{A27})$$

This is just the natural symmetric discretization of  $V_i = \sum_{\alpha} V_{i\alpha}$  with  $V_{i\alpha}$  given by Eq. (A8).

We have thus shown that the CTMC dynamics, with rates as in Eq. (13), is the natural discretization of overdamped Langevin dynamic in the continuum, and that CTMC becomes a very good approximation for the continuum dynamics in the limit that the energy changes for single particle moves,  $\Delta U_{i\alpha}$  of Eq. (A23), satisfy  $\Delta U_{i\alpha} \ll 2T$ .

\*Present address: Laboratory for Laser Energetics, University of Rochester, Rochester, NY 14627, USA.

†Present address: Department of Chemistry, University of Utah, Salt Lake City, UT 84112-0830, USA.

‡Present address: Department of Physics, MIT, Cambridge, MA 02139-4307, USA.

<sup>1</sup>For a review see, B. Schmittmann and R. K. P. Zia, in *Phase Transitions and Critical Phenomena*, edited by C. Domb and J. L. Lebowitz (Academic, New York, 1995), Vol. 17, and references therein.

<sup>2</sup>S. Katz, J. L. Lebowitz and H. Spohn, Phys. Rev. B **28**, 1655 (1983); J. Stat. Phys. **34**, 497 (1984).

<sup>3</sup>P. C. Hohenberg and B. I. Halperin, Rev. Mod. Phys. **49**, 435 (1977).

<sup>4</sup>A. B. Bortz, M. H. Kalos and J. L. Lebowitz, J. Comput. Phys. **17**, 10 (1975).

<sup>5</sup>M. E. J. Newman and G. T. Barkema, *Monte Carlo Methods in Statistical Physics* (Clarendon, Oxford, 1999); J. Dall and P. Sibani, Comput. Phys. Commun. **141**, 260 (2001).

<sup>6</sup>M. Franz and S. Teitel, Phys. Rev. B **51**, 6551 (1995).

<sup>7</sup>A recent work comparing Metropolis, Glauber, and heat bath Monte Carlo dynamics for a driven diffusive Ising lattice gas can be found in W. Kwak, D. P. Landau, and B. Schmittmann, Phys. Rev. E **69**, 066134 (2004). Here the different dynamics produced quantitative, but not qualitative, differences in the resulting steady states.

<sup>8</sup>V. Gotcheva, A. T. J. Wang and S. Teitel, Phys. Rev. Lett. **92**, 247005 (2004).

<sup>9</sup>J.-R. Lee and S. Teitel, Phys. Rev. B **46**, 3247 (1992).

<sup>10</sup>V. Ambegaokar and B. I. Halperin, Phys. Rev. Lett. **22**, 1364 (1969).

<sup>11</sup>In the very large drive limit  $F \gg U_0$ , when the work done by the force dominates over the change in interaction energy, it may be possible to choose  $W_0$  dependent on  $F$  (and possibly varying with grid direction  $\hat{a}_\mu$ ) in such a way as to again match onto the continuum solution. This remains for further investigation.

<sup>12</sup>M. de Berg, M. van Kreveld, M. Overmars and O. Schwarzkopf, *Computational Geometry* (Springer Verlag, Berlin, 1997).

<sup>13</sup>L. M. Jensen, B. J. Kim and P. Minnhagen, Phys. Rev. B **61**, 15412 (2000), see Appendix B.

<sup>14</sup>F. Reif, *Fundamentals of Statistical and Thermal Physics* (McGraw-Hill, New York, 1965).

<sup>15</sup>T. Giamarchi and P. Le Doussal, Phys. Rev. Lett. **76**, 3408 (1996); P. Le Doussal and T. Giamarchi, Phys. Rev. B **57**, 11356 (1998).

<sup>16</sup>W. H. Press, B. P. Flannery, S. A. Teukolsky, and W. T. Vetterling, *Numerical Recipes in C* (Cambridge University Press, Cambridge, 1988), see Chap. 7.6.

<sup>17</sup>K. Moon, R. T. Scalettar, and G. T. Zimányi, Phys. Rev. Lett. **77**, 2778 (1996).

<sup>18</sup>D. R. Nelson and B. I. Halperin, Phys. Rev. B **19**, 2457 (1979); A. P. Young, Phys. Rev. B **19**, 1855 (1979).

<sup>19</sup>L. Balents, M. C. Marchetti, and L. Radzihovsky, Phys. Rev. Lett. **78**, 751 (1997); Phys. Rev. B **57**, 7705 (1998).

<sup>20</sup>S. Scheidl and V. M. Vinokur, Phys. Rev. E **57**, 2574 (1998).

<sup>21</sup>A. E. Koshelev and V. M. Vinokur, Phys. Rev. Lett. **73**, 3580 (1994).

<sup>22</sup>M. C. Faleski, M. C. Marchetti, and A. A. Middleton, Phys. Rev. B **54**, 12 427 (1996).

<sup>23</sup>S. Ryu, M. Hellerqvist, S. Doniach, A. Kapitulnik, and D. Stroud, Phys. Rev. Lett. **77**, 5114 (1996).

<sup>24</sup>S. Spencer and H. J. Jensen, Phys. Rev. B **55**, 8473 (1997).

<sup>25</sup>D. Domínguez, Phys. Rev. Lett. **82**, 181 (1999).

<sup>26</sup>A. B. Kolton, D. Domínguez, and N. Grønbech-Jensen, Phys. Rev. Lett. **83**, 3061 (1999).

<sup>27</sup>H. Fangohr, S. J. Cox, and P. A. J. de Groot, Phys. Rev. B **64**, 064505 (2001).

<sup>28</sup>C. Reichhardt and G. T. Zimányi, Phys. Rev. B **61**, 14 354 (2000).

<sup>29</sup>G. Carneiro, Phys. Rev. B **62**, R14 661 (2000); **66**, 054523 (2002).

<sup>30</sup>V. I. Marconi and D. Domínguez, Phys. Rev. Lett. **82**, 4922 (1999).

<sup>31</sup>V. I. Marconi and D. Domínguez, Phys. Rev. B **63**, 174509 (2001).

<sup>32</sup>Marconi and Domínguez in Ref. 31 also report a floating solid

phase that is *not* transversely pinned, and lies between the liquid and transversely pinned solid phases. However, there are indications that this fully unpinned solid phase may vanish in the limit of longer simulation times; D. Domínguez (private communication).

- <sup>33</sup>C. J. Lobb, D. W. Abraham, and M. Tinkham, Phys. Rev. B **27**, 150 (1983).
- <sup>34</sup>A. B. Kolton, R. Exarter, L. F. Cugliandolo, D. Domínguez, and N. Grønbech-Jensen, Phys. Rev. Lett. **89**, 227001 (2002).
- <sup>35</sup>S. Teitel, Phys. Rev. B **39**, 7045 (1989).